RSC Advances

PAPER

View Article Online
View Journal | View Issue

Cite this: *RSC Adv.*, 2020, **10**, 25239

New nanosized Gd–Ho–Sm doped M-type strontium hexaferrite for water treatment application: experimental and theoretical investigations

M. Elansary,[a] M. Belaiche,*[a] C. Ahmani Ferdi,[a] E. Iffer[a] and I. Bsoul[b]

In this paper, rare-earth doped M-type strontium hexaferrite magnetic nanoparticles $SrHo_xGd_ySm_z$-$Fe_{(12-(x+z+y))}O_{19}$ ($x = y = z = 0.01$) have been prepared by the sol–gel combustion method for the first time. The properties of the material were investigated using XRD, FTIR spectroscopy, Raman spectroscopy, SEM, UV-Vis spectroscopy, and VSM. X-ray analysis revealed that a magnetic single-phase was formed with a crystallite average size of 49 nm. FTIR spectra confirmed the formation of the structure of the hexaferrite phase. Raman analysis confirmed the formation of all crystallographic hexaferrite sites. A shift in the octahedral site frequencies and a significant shift were observed at site 12k and 2a, indicating that the doping elements occupied these sites. The SEM analysis showed that the particles were different in shape and slightly agglomerated. The EDS result confirmed the purity of the sample. The calculated band gap from the UV-Vis NIR spectroscopy spectra of the sample was 1.62 eV. The magnetic analysis of the sample material at room temperature revealed a coercivity of 5257.63 Oe, saturation magnetization of 67.72 emu g^{-1}, remanence ratio of 0.52, a maximum magnetic energy product of 1.06 MGOe and Curie temperature of $T_c = 765$ K. First-principles calculations were conducted on multiple configurations of $SrFe_{12-x}X_xO_{19}$ with $x = 0$, 0.5 and X = Sm, Gd, Ho. The site preference of each doping element was determined, and the effect of the doping on the structural, electronic, and magnetic properties of the compound was studied. The magnetic properties of this rare earth (Gd, Ho, Sm) doped strontium hexaferrite indicated that this compound could be used in both permanent magnets and water treatment application.

Received 28th May 2020
Accepted 18th June 2020

DOI: 10.1039/d0ra04722h

rsc.li/rsc-advances

1. Introduction

Nanoscience has been a challenge in past years. It has allowed the design and prediction of the construction of sophisticated materials and devices by controlling and optimizing the functionality of matter at the nanometer scale. At this scale, new properties (physical, chemical and biological) can emerge that are fundamentally different from the properties in the bulk state. The field of nanoscience consists of innovating, modulating, shaping, and creating new nanostructures, and also discovering, determining, and understanding their new properties with a view to develop new, more useful, and complex functional devices. The challenge is to create a synergy between properties to have multifunctional devices. This is the introduction to a larger extent of the modern integrated interdisciplinary science currently known as nanotechnology, which is constantly developing.

Hexaferrite is still by far the most relevant material for practical applications, and currently constitutes the vast majority of hard ferrite production. They are extremely interesting materials for innumerable applications. Of particular interest is the strontium hexaferrite, which has attracted the interest of many researchers owing to their new electromagnetic properties, and their use in a wide range of applications. This is because it is characterized by a high saturation magnetization, a large coercive force, high Curie temperature, large magneto-crystalline anisotropy, high corrosion resistance and chemical stability.[1–3] Due to the qualities listed previously and its low cost, strontium hexaferrite is considered to be a favorite candidate for permanent magnets used for industrial applications that are environmentally friendly, such as generator rotors used in electric vehicles[4] or wind energy.[5] Such specific properties of these Sr-hexaferrite nanomaterials give them new physical and chemical functionalities for magnetic water treatment.[6,7] Scientists are more interested in the benefits of magnetically treated water in ensuring the quantity of seeds

[a]*Nanomaterials and Nanotechnology Unit, E. N. S Rabat, Energy Research Centre, Faculty of Sciences, Mohammed V University, B. P. 5118 Takaddoum Rabat, Morocco. E-mail: med.belaiche@um5.ac.ma*

[b]*Physics Department, Al al-Bayt University, Mafraq 13040, Jordan*

needed for planting, shortening the growth phase, reducing plant diseases, and providing water for irrigation. The current studies in this field are focused on understanding this phenomenon since the physical pathways are efficient and increase efficiency with respect to the environment.[8] In addition, strontium hexaferrite is also used in bonded magnets, in various microwave devices (isolator, circulators, filters, phase shifters) and magnetic and magneto-optic recorders of information with high density.[9–12]

Ferrite magnets may not be as powerful as rare earth magnets (SmCo and NdFeB) and rare earth alloys due to their desired magnetic properties. However, due to the price volatility and supply-chain vulnerability of rare earth materials, researchers all over the world are making an effort to overcome the problem of producing novel magnetic materials with free rare-earth content akin to rare earth magnets.[13] Strontium hexaferrite (**SrM**) has the advantage of a high Curie temperature of 733 K, compared to commercial NdFeB (583 K).[14] They also remain the most widely used magnets due to their low production cost.

For application in magnetic water treatment, a high remanence, high coercivity, and large energy product $(BH)_{max}$ are required. To obtain these properties, a small grain size, growth anisotropy, and high-density ferrite are imperative. The upgrading of the energy product $(BH)_{max}$ is more delicate than the improvement of coercivity. A higher density ferrite with uniform grain distribution can improve the magnetic properties. However, researchers are now attempting to explore the magnetic properties by changing the stoichiometry, chemical purity, and the processing conditions of the material. Substitutions of the Sr^{2+} and Fe^{3+} cations are the best way to find productive compositions for various applications. Previous works have studied the substitution of Fe^{3+} ions of strontium hexaferrite by different cations, such as Ho^{3+}, Ti^{4+}, Al^{3+}, Cr^{3+}, and Ga^{3+}.[15–19] Some are substituted by other elements, such as La^{3+}, Nd^{3+}, Sm^{3+}, Pr^{3+}, and Gd^{3+}.[20–24] They have been carried out to obtain the appropriate magnetic properties. Afterward, the combined substitution (such as Mn–Sn–Ti, Zn–Nb, La–Cu[25–27]) has been achieved successfully in M-type hexagonal ferrites using different synthesis methods. The main techniques of preparing strontium hexaferrite include the sol–gel process,[28] co-precipitation method,[29] self-propagation,[30] the mechanical alloying methods,[31] microwave,[32] hydrothermal,[33] and ultrasound-assisted synthesis.[34] In this study, the sol–gel method was used to synthesize Sr hexaferrite. It is an effective process to produce ferrites due to its low cost, and the ability to produce fine and homogeneous crystalline powders without any risk of contamination.[35]

The aim of this work is focused on the enhancement of the magnetic properties of $SrFe_{12}O_{19}$, especially the energy product $(BH)_{max}$, to be applied in magnetic water treatment. In this work, $Sr(Ho_xGd_ySm_z)Fe_{(12-(x+z+y))}O_{19}$ ($x = y = z = 0.01$) was prepared by doping with small amounts of Sm^{3+}, Gd^{3+}, and Ho^{3+} ions simultaneously into $SrFe_{12}O_{19}$, using the sol–gel method. To our knowledge, no similar work has been reported.

The magnetic properties of $Sr(Ho_xGd_ySm_z)Fe_{(12-(x+z+y))}O_{19}$ ($x = y = z = 0.01$) (labeled **RE.SrM**) were investigated and the substitution mechanism of Sm^{3+}, Gd^{3+} and Ho^{3+} ions were discussed in detail. First-principles calculations were conducted on the different configurations of $SrFe_{12-x}X_xO_{19}$ with $x = 0$, 0.5 and X = Sm, Gd, Ho to shed light on the effects of doping the M-type strontium hexaferrite with the rare-earth elements Sm, Gd, and Ho on its structural, electronic and magnetic properties. This work aims to provide new ideas on the elaboration of magnetic samples suitable for specific applications, and to explain the effect of rare-earth doping on the magnetic properties of $SrFe_{12}O_{19}$.

2. Experimental and computational details

2.1. Computational details

The calculations for the structural optimization were performed using density functional theory with projector-augmented wave (PAW) potentials, as implemented in the Quantum Espresso plane-waves density functional theory package.[36] The exchange–correlation potential was approximated by the Perdew–Burke–Ernzerhof Generalized Gradient Approximation (GGA).[37] A $5 \times 5 \times 1$ Monkhorst–Pack k-mesh and a 612 eV energy cut-off were used.[38] The atomic positions, cell shape and cell volume of all compounds were fully relaxed using the Broyden–Fletcher–Goldfarb–Shanno (BFGS) algorithm until the forces were below 1 mRy per bohr (Ry: Rydberg). The obtained cell parameters and atomic positions were used to calculate their total energies, as well as their electronic and magnetic properties, using the Wien2k package.[39] The ion-electron interaction was described with the Full-Potential Linear Augmented Plane Wave (FP-LAPW) method. The exchange–correlation potential was approximated by the Perdew–Burke–Ernzerhof Generalized Gradient Approximation (GGA).[37] Fe has been assigned a U_{eff} parameter ($U_{eff} = U - J$) to correct for the self-interaction error present in GGA.[40] The U_{eff} parameter was applied on the Fe 3d electrons in all of the GGA+U calculations, and the used values for the U_{eff} parameter were 3, 4 and 6 eV. The Muffin Tin Radii (MTR) were chosen to ensure a nearly touching sphere, and to minimize the interstitial space. The plane-wave cut-off was defined by $Rk_{max} = 6.5$. The Brillouin zone (BZ) was sampled with at least 1900 k-points/(number of atoms in the unit cell). The Fermi energy was calculated using a temperature-broadening scheme, with a broadening parameter of 0.002 Ry. The energy threshold between the core and the valence states was set at −6.81 eV. The convergence criteria for energy were chosen to be 10^{-5} Ry. All calculations were spin-polarized according to the following ground state ferrimagnetic ordering of the Fe spins: [12k(↑), 2a(↑), 2b(↑), $4f_1$(↓), $4f_2$(↓)]. ((↑) indicates spin up and (↓) indicates spin down).

2.2. Experimental details

The series of M-type Sr hexaferrite $Sr(Ho_xGd_ySm_z)Fe_{(12-(x+z+y))}O_{19}$ ($x = y = z = 0.01$) (**RE.SrM**) were prepared by the sol–gel combustion method. The chemicals strontium nitrate, $Sr(NO_3)_2$ (≥98.0% pure, Sigma-Aldrich), ferric nitrate nonahydrate $Fe(NO_3)_3 \cdot 9H_2O$, samarium nitrate hexahydrate $Sm(NO_3)_3 \cdot 6H_2O$

(≥99.0% pure, Sigma-Aldrich), gadolinium nitrate hexahydrate $Gd(NO_3)_3 \cdot 6H_2O$ (≥99.0% pure, Sigma-Aldrich), holmium nitrate pentahydrate $Ho(NO_3)_3 \cdot 5H_2O$ (≥99.0% pure, Sigma-Aldrich) and citric acid ($C_6H_8O_7$) were used as raw materials to prepare the (**RE.SrM**) nanoparticles. The appropriate amounts of nitrates were dissolved in distilled water under magnetic stirring for 30 minutes, and then citric acid was dissolved in it with a molar ratio of nitrates to citric acid of 1 : 2. Ammonia solution was added drop-wise into the solution to adjust the pH values at 1.5, 4 and 7, while stirring at 70 °C continuously until the solution changed into the gel. When the gel formation started, we heated the gel at 200 °C until we acquired a fluffy powder. Then, the powder was ground using an agate mortar and pestle. After grinding, the powder was placed overnight in an oven to dry it completely at 100 °C. Then, the powder was ground once again. Finally, the homogenized powder was then calcined at 700 °C, 800 °C, 900 °C and 1000 °C.

3. Results and discussion

3.1. Phase identification analysis

Fig. 1 shows the XRD pattern of the samples sintered at different temperatures and pH values. The XRD patterns reveal single-phase M-type Sr hexaferrite, which is matched with the ICDD file number 96-100-8857 and confirm the formation of crystalline structures. The diffraction peaks are mainly indexed to the M-type Sr hexaferrite phase. Furthermore, a small additional secondary phase (Fe_2O_3) was detected at pH = 1.5 (700 °C, 800 °C, 900 °C), pH = 4 (700 °C) and pH = 7 (700 °C). The XRD patterns clearly show that the peak intensities of Fe_2O_3 disappear at 1000 °C for all different pH values. This can be explained by the nucleation, growth of grains and a complete crystallization of the M-type Sr hexaferrite. No diffraction peaks from any second impurity phases were observed at 1000 °C for the different pH values. This indicates that the M-type Sr hexaferrite formation is promoted by increasing the temperature and pH. Therefore, the temperature value of 1000 °C and pH = 7 were selected as the optimum conditions.

Fig. 2 shows the XRD patterns of the (**RE.SrM**) nanoparticles calcined at 1000 °C and with a pH value of 7. The main peaks of the M-type Sr hexaferrite were at 2θ = 30.40, 31.04, 32.38, 34.24, 37.20, 38.57, 40.48, 42.66, 55.32 and 63.28, revealing the typical hexagonal planes of (110), (008), (107), (114), (203), (116), (205), (206), (214), and (220), respectively. The spectrum confirms the high crystallization of the sample, and reveals that the Sm^{3+}, Gd^{3+} and Ho^{3+} ions go into the lattice of the type M hexaferrite.

All XRD patterns of all samples have been analyzed employing Rietveld refinement with the help of the FullProf Suite software. During the refinement, the zero correction, scale factor, atomic position, lattice parameters, line widths, and thermal parameters were refined simultaneously. The shape of the peaks was described by the pseudo-Voigt function, and the

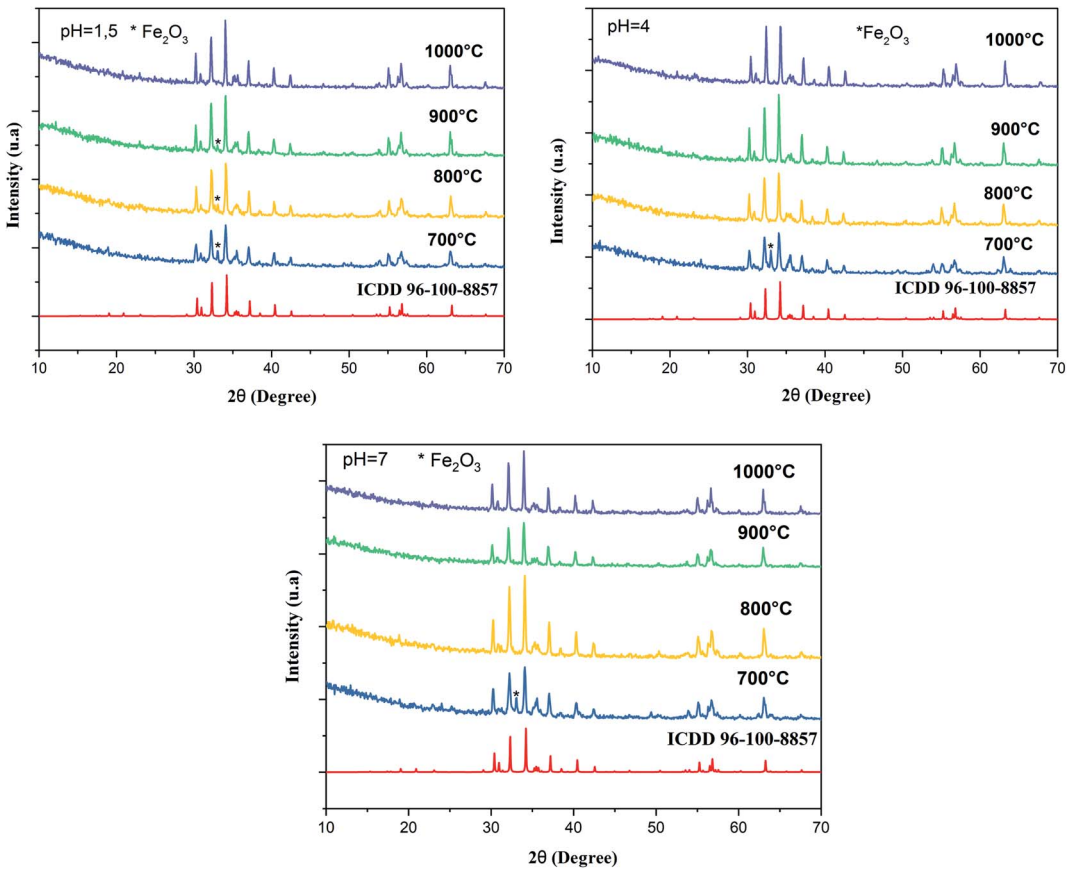

Fig. 1 Indexed X-ray diffraction pattern of $SrFe_{12}O_{19}$ particles at different pH values and different calcination temperatures.

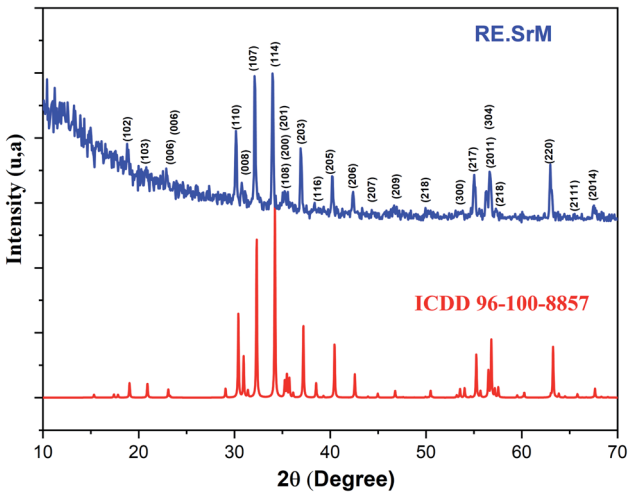

Fig. 2 Indexed X-ray diffraction pattern of (**RE.SrM**).

background was expressed by a linear interpolation between a set of selected background points. The fitting was judged by the goodness of fit, along with the low values of reliable factors (χ^2) as included in Table 1. It could be seen that the profiles for the observed and calculated ones are perfectly matched with each other and all the experimental peaks.

The Rietveld refinement of the room temperature powder XRD patterns of all hexaferrite samples is shown in Fig. 3, all peaks in the XRD patterns were indexed to M-type hexagonal structure with space group $P6_3/mmc$. The refined lattice parameter values and cell volume (v) of the intrinsic M-type Sr hexaferrite are given in Table 1. The lattice constant values (a) and (c) are found in the range of (a = 5.8665–5.8807 Å) and (c = 22.9985–23.0657 Å), respectively. These values are comparable to the standard values ($a = b$ = 5.8862 Å) (c = 23.1370 Å),[41] and in good agreement with the values found by Azis *et al.*[42] The volume of the cells was found in the range of (V = 688.9894–690.8272 Å^3) for all sintered samples. The c/a values vary from 3.9188 to 3.9222. These values are comparable to the standard value (3.9800) of the M-type hexagonal structure.[43]

As shown in Fig. 4 of the Rietveld refined XRD pattern of (**RE.SrM**), narrow and well-defined peaks corresponding to the M-type Sr hexaferrite were observed in the samples, indicating the formation of the highly crystalline M-type Sr hexaferrite phase.

The structural parameters obtained from the Rietveld refinement of (**RE.SrM**) are given in Table 1. The obtained (a) and (c) lattice constants are 5.8734 Å and 23.0236 Å for (**RE.SrM**), respectively. These results confirm that no structural change occurs in the M-type Sr hexaferrite upon doping with Sm^{3+}, Gd^{3+}, and Ho^{3+} ions. On the other hand, from Table 1, it can be noticed that the lattice parameter remains almost constant and c has been decreased compared to the undoped M-type Sr hexaferrite. Generally, the insertion of higher ionic radii elements in the host lattice swells the crystal lattice. However, the opposite behavior has been observed in the present work. Such behaviour can be attributed to many factors. In particular, the low solubility of the rare earth substitution in strontium hexaferrite can induce the formation of secondary phases. But, in the present case, no secondary phase has been observed, and the case to be excluded as a pure single phase was obtained. Otherwise, this anomaly can only be attributed to the bonding energy and exchange interaction. In fact, the introduction of small quantities of larger rare earth elements can induce strong interactions between neighboring atoms, which leads to a stress of the crystal lattice resulting from a cationic redistribution of ions in the host lattice. Consequently, the crystal lattice reduces in size and the lattice parameters decrease. A similar behavior has been observed in the literature.[44,45] The presence of 4f electrons with 5d electrons in the lanthanides leads to stronger Colombian attractions that form a strong oxygen–lanthanide (R–O) bond in the crystal structure. Transition metal ions have only 5d electrons. Therefore, they have weaker transition metal–oxygen (M–O) bonds in the crystal structure. In the RE-doped hexaferrite, the binding energy of the oxygen–lanthanide octahedron (RO_6) is higher than the oxygen-cation octahedron of the transition metal (MO_6).[46,47] As a result, the crystal lattice of the RE-substituted strontium hexaferrite can contract so that the values of a, c and the V-cell decrease as observed.

Table 1 Structural parameters for $SrFe_{12}O_{19}$ and (**RE.SrM**)

	pH	Calcination temperature (°C)	a (Å)	c (Å)	Cell volume (Å^3)	c/a	Crystallite size (nm)	Density (g cm^{-3})	χ^2
$SrFe_{12}O_{19}$	1.5	700	5.880	23.065	690.82	3.922	33	5.104	1.19
		800	5.878	23.058	690.13	3.921	43	5.105	1.29
		900	5.875	23.042	689.08	3.921	54	5.117	1.43
		1000	5.877	23.038	689.02	3.920	62	5.117	1.29
	4	700	5.879	23.057	690.12	3.921	33	5.109	1.38
		800	5.879	23.052	690.13	3.920	42	5.109	1.29
		900	5.878	23.039	689.38	3.919	47	5.115	1.33
		1000	5.883	23.053	690.97	3.918	48	5.103	1.43
	7	700	5.878	23.047	689.57	3.921	35	5.113	1.29
		800	5.877	23.035	688.98	3.919	45	5.117	1.28
		900	5.866	22.998	685.47	3.920	44	5.144	1.33
SrM	7	1000	5.876	23.035	688.89	3.920	53	5.118	1.29
RE.SrM		1000	5.872	23.023	687.84	3.91	49	5.126	1.26

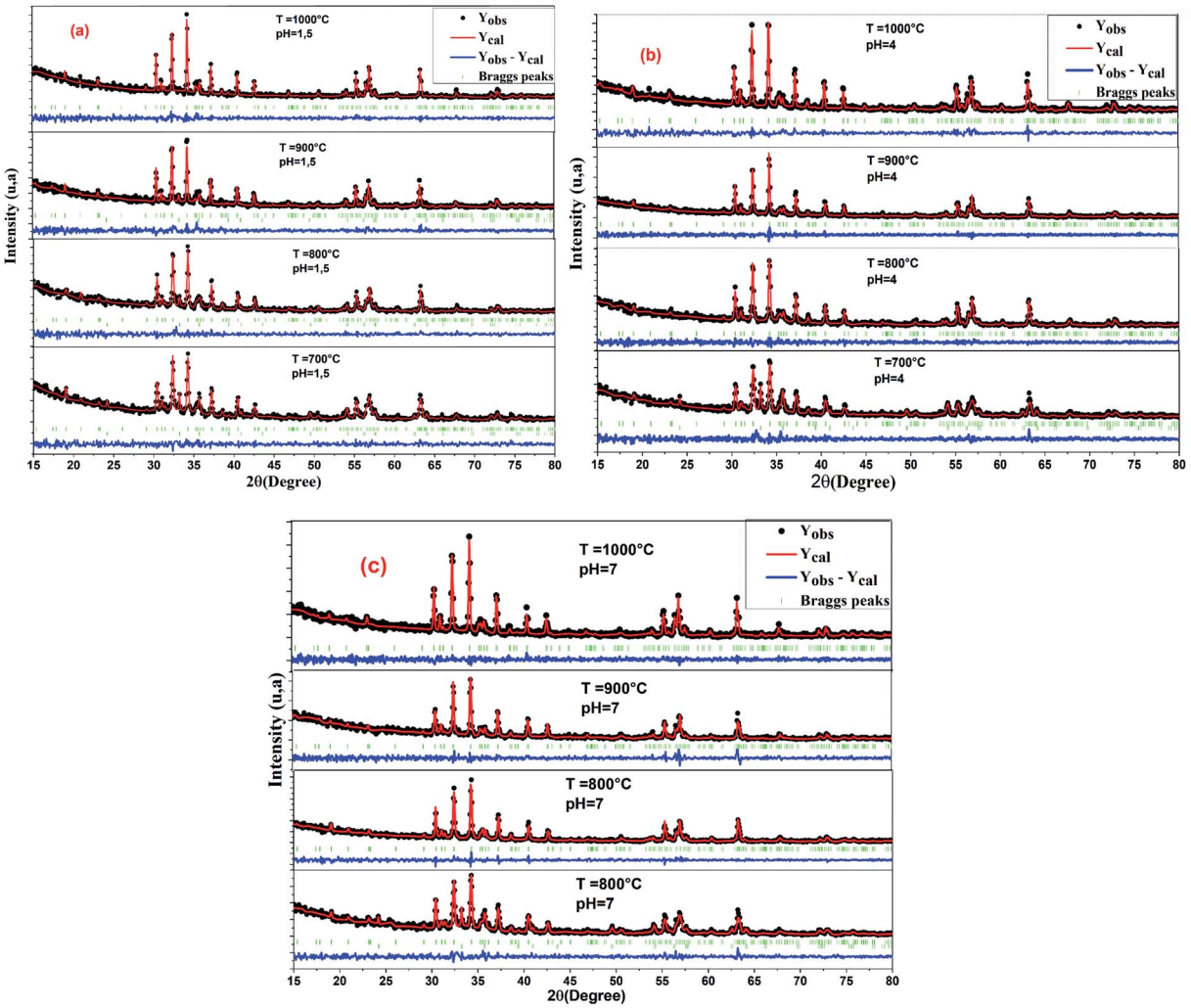

Fig. 3 Rietveld refinement patterns of all un-doped samples of $SrFe_{12}O_{19}$, (a) pH = 1.5, (b) pH = 4, and (c) pH = 7.

Indeed, the refined ionic positions in the doped sample exhibited shifts relative to the undoped sample at the sites (12k) for Fe^{3+}, and also in the (6h) and (12k) sites for O^{2-} as shown for both in Table 2. These displacements are due to the Gd^{3+}, Ho^{3+}, and Sm^{3+} ions that are forced to occupy the octahedral sites, owing to their preferred site energy. In addition, the length of the Fe–O bond at the octahedral and tetrahedral sites is reduced relative to the average length of the bond at the bipyramidal sites. This indicates that the bond length at the sites is decreased due to the introduction of small quantities of rare-earth materials into the hexaferrite. This decrease is due to the improvement in the exchange interactions. It should also be noted that a significant deviation of the binding angles was observed in the doped sample compared to the undoped sample (Table 3). The details of this deviation will be discussed in the magnetic discussion section.

The effect of the pH value and calcination temperature on the crystallite sizes was studied. The crystallite sizes of the samples were calculated using the Debye–Scherrer formula:[48]

$$D_{XRD} = \frac{0.9\lambda}{\beta \cos \theta} \quad (1)$$

where D_{XRD} is the average size of the crystallites, θ is the Braggs diffraction angle, β is the full-width half-maximum (in radians), and λ is the wavelength of the X-rays used (1.5406 Å). Fig. 5(b) shows the effect of various annealing temperatures on the crystalline size of the obtained powders for different pH values. We note that the increase in the annealing temperatures significantly promotes particle agglomeration and grain growth during calcination, which leads to the increase of grain size and the formation of M-type Sr hexaferrite powders. From Fig. 5(a), the results show that as the pH increases, the crystallite sizes decrease in full agreement with the results obtained by Wu *et al.*[49]

The crystallite sizes of (**RE.SrM**) decreased compared to that of the (**SrM**). This decrease in crystallite size can be explained by the high bond energy of Sm^{3+}–O^{2-}, Gd^{3+}–O^{2-} and Ho^{3+}–O^{2-} as compared to that of Fe^{3+}–O^{2-}. Therefore, more energy is required for the formation of the bonds of rare earth elements in the M-type Sr hexaferrite. This required energy was obtained

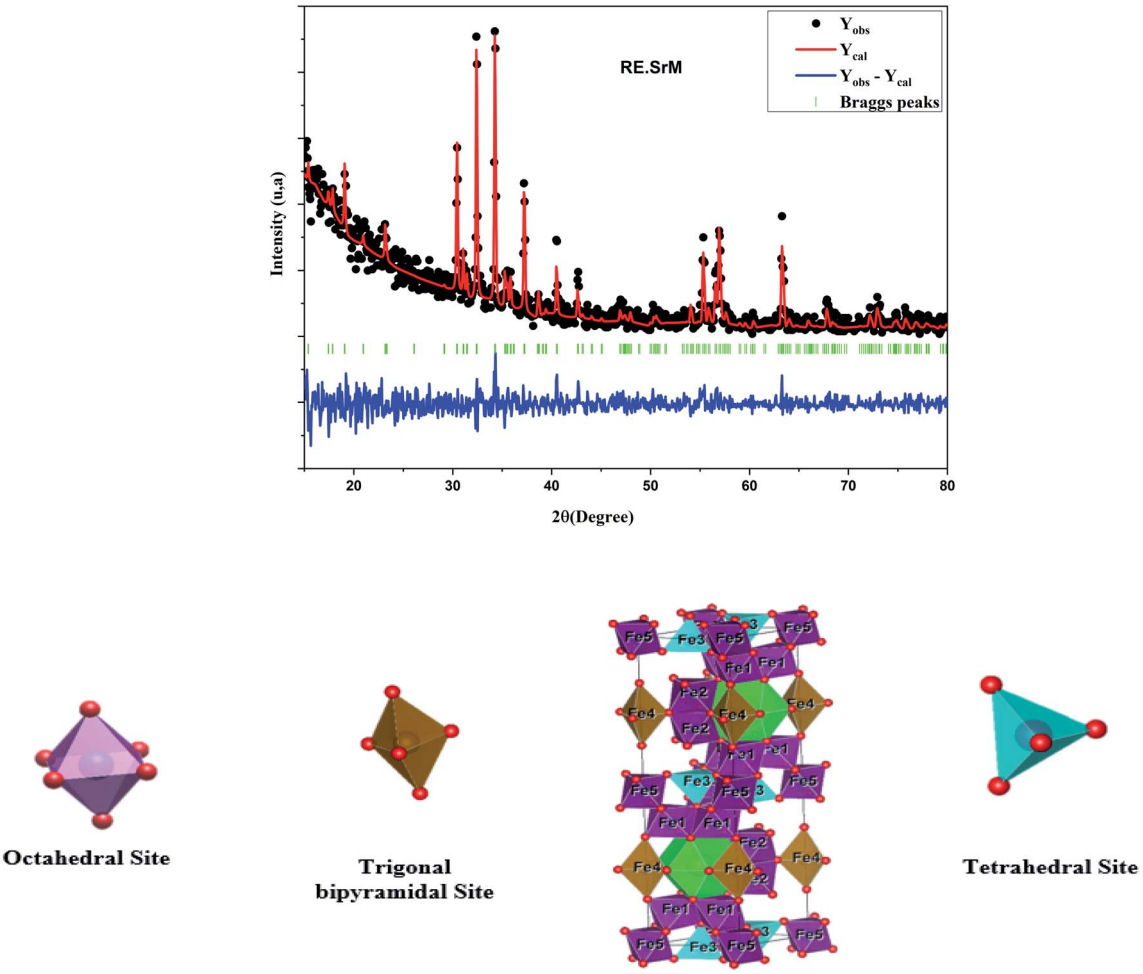

Fig. 4 Rietveld refinement patterns of (RE.SrM) and schematic of hexaferrite.

Table 2 Atomic positions obtained from the Rietveld refinement for the $SrFe_{12}O_{19}$ and (RE.SrM) samples

		x/*a*		*y*/*b*		*z*/*c*	
Atom	Site	SrM	RE.SrM	SrM	RE.SrM	SrM	RE.SrM
Sr	2d	0.66667	0.66667	0.33333	0.33333	0.25000	0.25000
Fe1	2a	0.00000	0.00000	0.00000	0.00000	0.00000	0.00000
Fe2	2b	0.00000	0.00000	0.00000	0.00000	0.25000	0.25000
Fe3	$4f_1$	0.33333	0.33333	0.66667	0.66667	0.02710	0.02000
Fe4	$4f_2$	0.33333	0.33333	0.66667	0.66667	0.30890	0.30770
Fe5	12k	0.17200	0.16667	0.34400	0.33333	0.88950	0.89014
O1	4e	0.00000	0.00000	0.00000	0.00000	0.16500	0.15350
O2	4f	0.33333	0.33333	0.66667	0.66667	0.93500	0.94000
O3	6h	0.18600	0.21198	0.37100	0.42389	0.25000	0.25000
O4	12k	0.16000	0.18650	0.84000	0.81350	0.05600	0.05339
O5	12k	0.48900	1.43274	−0.02200	1.86548	0.15350	0.15000

at the expense of crystallization, and consequently caused a hindrance in the growth of the crystallite of the M-type Sr hexaferrite.[50] This may be explained on the basis of ionic radii or lattice contraction. The reduction in the crystallite size probably decreases the crystal axis ratio. These results also suggest that the Sm^{3+}, Gd^{3+}, and Ho^{3+} have systematically entered the host lattice in place of Fe^{3+}.

3.2. FT-IR spectrum

FTIR spectroscopy makes it possible to predict the presence of the different bonds in a crystal. FTIR analysis was performed at room temperature in the range of 400–4000 cm^{-1}, and is represented in Fig. 6. The frequency absorption bands at 584.82 cm^{-1} and 422.71 cm^{-1} correspond to the tetrahedral and octahedral Fe^{3+}–O stretching vibrations, respectively, and the characteristic peaks at 539.86 cm^{-1} are associated with the Sr–O stretching vibration band.[51] FTIR analysis of the samples confirmed the formation of the M-type Sr hexaferrite. No parasitic bands in all samples were observed. Thus, we can make a preliminary deduction that the added low concentration of Sm^{3+}, Gd^{3+} and Ho^{3+} ions did not alter the intrinsic structure of the M-type Sr hexaferrite, which is in good agreement with the XRD results.

3.3. Raman analysis

The Raman spectra can give us more information on the dynamics of the crystal structure. The peaks in the Raman

Table 3 Different (Me–O) bond lengths and bond angles of Me1–O–Me2 for (SrM) and (RE.SrM)

		Bond length (Å)	
Site	Bond type	SrM	RE.SrM
Fe1 (2a)	Fe1–O4	2.14	2.26
Fe2 (2b)	Fe2–O1	1.93	2.22
	Fe2–O3	1.19	2.17
Fe3 ($4f_1$)	Fe3–O2	2.23	1.84
	Fe3–O4	1.84	1.68
Fe4 ($4f_2$)	Fe4–O3	2.00	1.80
	Fe4–O5	1.87	1.40
Fe5 (12k)	Fe5–O1	2.16	1.96
	Fe5–O2	1.90	2.04
	Fe5–O4	2.11	2.22
	Fe5–O5	1.97	1.93
	Sr–O3	2.91	2.97
	Fe4–Fe4	2.59	2.66
	Fe5–Fe5	2.83	2.93

	Bond angles	
Bond type	SrM	RE.SrM
Fe1–O4–Fe3	120.19	119.83
Fe1–O4–Fe5	93.88	85.51
Fe2–O1–Fe5	126.00	120.65
Fe2–O3–Fe4	139.48	132.91
Fe3–O2–Fe5	120.84	124.09
Fe4–O3–Fe4	81.04	94.19
Fe4–O5–Fe5	132.18	138.91
Fe5–O2–Fe5	96.06	91.63
Fe5–O5–Fe5	92.34	87.75

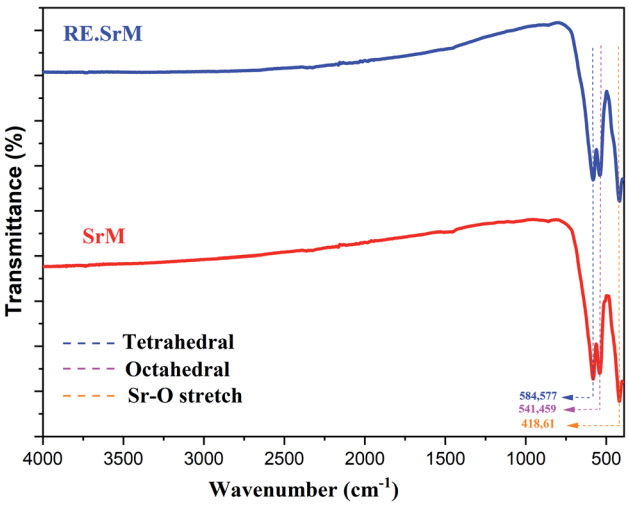

Fig. 6 FT-IR spectra of (SrM) and (RE.SrM).

spectra are mainly related to the vibration of the atomic bond. Therefore, a small amount of impurities can be detected. In parallel, Raman spectroscopy was used to study the composition and homogeneity of the phases in the pure and rare-earth doped $SrFe_{12}O_{19}$ system. The Raman spectra are shown in Fig. 7. Raman spectral analysis of the pure and rare-earth doped strontium hexaferrite were carried out by comparing the observed results with the selection rules and mode assignments discussed by Kreisel *et al.*[52] From the literature, it was reported that 42 Raman-active modes ($11A_{1g} + 14E_{1g} + 17E_{2g}$) and 30 IR active modes ($13A_{2u} + 17E_{1u}$) are expected for the hexaferrite system. The Raman spectra were determined at room temperature. The hexagonal structure of the M-type strontium hexaferrite was built up of five layers: 3 cubic blocks of S and S* with a spinel structure, and 2 hexagonal blocks R and R* containing the Sr^{2+} ion. These five layers form one molecule, and two molecules form one unit cell. The 24 Fe^{3+} ions are distributed over five different crystallographic sites, three octahedral positions (12k, 2a and $4f_2$), one tetrahedral position ($4f_1$) and one trigonal-bipyramidal (2b) position, respectively. The Raman spectra of the doped and undoped samples are shown in Fig. 7, and all have the strongest peak at approximately 679 cm^{-1}, which is attributed to the motions (A_{1g}) of the bipyramidal group of the Fe–O ions (site 2b).[52] A weak peak was observed at the frequency of 719 cm^{-1}, which can be attributed to the movement (A_{1g}) of the Fe–O ions at the $4f_1$ tetrahedral sites. The 608 cm^{-1} and 523 cm^{-1} bands are due to the (A_{1g}) and (E_{2g}) vibration modes of the Fe–O bonds at the $4f_2$ octahedral site. The 505 cm^{-1} and 463 cm^{-1} bands are due to the A_{1g} vibration

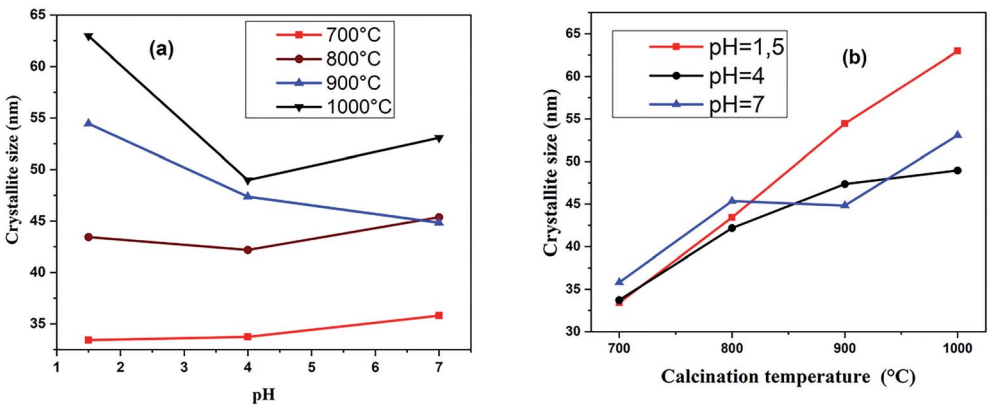

Fig. 5 Variation of crystallite sizes with pH value (a) and calcination temperature (b).

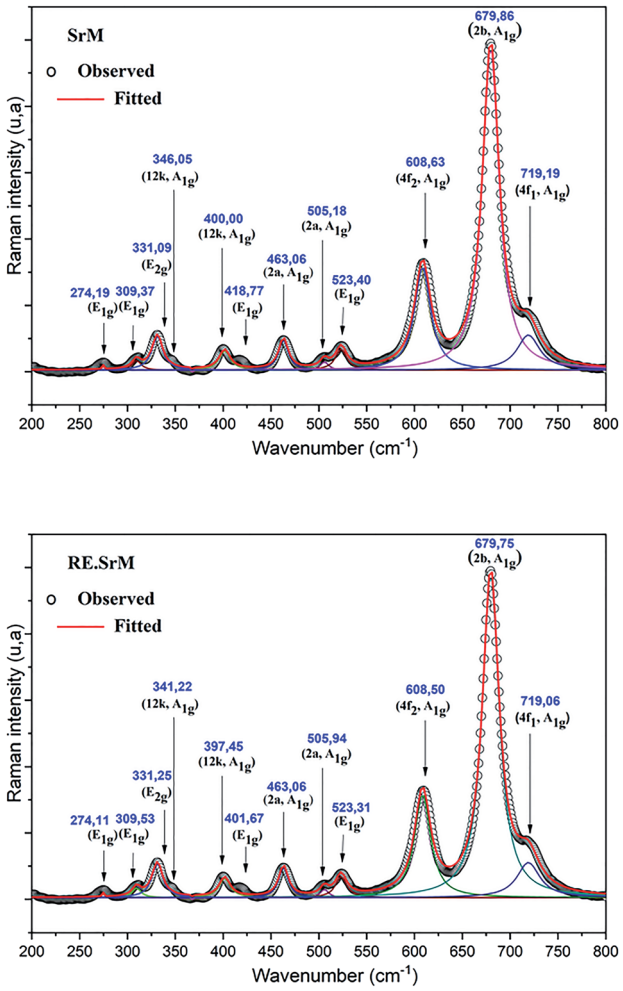

Fig. 7 Raman spectra of (RE.SrM) and (SrM) at room temperature.

modes of the Fe–O bonds at the 2a octahedral site. In addition to the above peaks, several distinct peaks are observed for the two samples corresponding to the frequencies of 317, 336, 415, 466 and 529 cm^{-1}. They are comparable to the Raman spectra reported by Zhao *et al.*, in samples of $BaFe_{12+x}O_{19+1.5x}$.[53] The bands in the 211 to 529 cm^{-1} regions can be attributed to the vibration of all M–O (M = Fe, Gd, Ho, Sm) bonds in various octahedral positions, such as 12k, 2a, and $4f_2$ sites. The measured Raman spectra of the two samples show that, other than the broadening of various bands, no new band was observed. This confirms that the samples are in a single-phase form.

In order to better correlate the Raman measurements with the cationic structure and distribution, the volumes of the different sites in the hexagonal lattice were determined. From the data refined by Rietveld, the available site volumes were calculated for both compounds. Table 4 shows the volumes available for the corresponding sites. From the volume values, it can be concluded as a first approximation that in the case of substitution, it seems that the $4f_2$, $4f_1$ and 2b sites are the most improbable to be substituted with Gd, Ho, and Sm. These results are in very good agreement with the Raman measurements. In fact, the sites undergoing a significant shift are the two sites 12k and 2a (see table: Raman shift). So the most probable sites to be substituted by Gd^{3+}, Ho^{3+}, and Sm^{3+} are the two sites 12k and 2a. The larger volume of available sites certainly plays a major role in site preference. However, the substitution energy may also contribute to site preference. In this context, using the present *ab initio* calculations with the GGA+U method (ample details of the calculations are elucidated in the last paragraph), the substitution energies in the 12k, 2a and $4f_2$ sites of the rare-earth elements Gd, Ho, Sm were calculated for $U_{eff} = 3, 4, 6$. From the obtained results, it can be seen that the minimum energy required for an Sm atom is to substitute Fe atoms in a 2a site, and the 12k site is the preferable site to be substituted with Gd and Ho atoms.

In order to analyze the polarization dependence of the Raman signals, the Raman bands were fitted with the Lorentzian line shape using the Raman bands. The results are shown in Fig. 7. The observed Raman spectra have been indexed, and the comparative state of the observed vibration

Table 4 Volume of the crystallographic sites of (SrM) and (RE.SrM)

		Octahedral sites			Tetrahedral site	Tirgonal bipyramodal site
		12k	2a	$4f_2$	$4f_1$	2b
		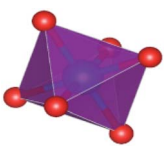	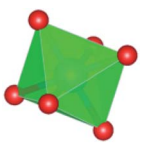	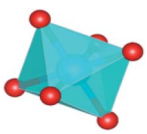	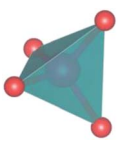	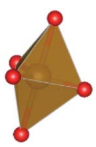
SrM	Volume $(Å)^3$	11.3865	11.8511	9.197	3.7566	6.9056
	Average bond length (Å)	1.9864	2.0775	1.9500	1.9446	1.9056
(**RE.SrM**)	Volume $(Å)^3$	10.5585	9.9155	8.5612	3.9322	8.9451
	Average bond length (Å)	2.0051	1.9595	1.8612	1.9734	2.1824
M–Sr theory	Volume $(Å)^3$	10.9145	9.6653	9.9599	3.5058	6.5139
	Average bond length (Å)	2.0215	1.9375	1.9709	1.8983	1.9874

Table 5 The observed Raman shift and assignment to the crystal site and symmetry for the (RE.SrM) and (SrM) samples

	Wavenumber					
Site	M–Sr	(**RE.SrM**)	|ΔRaman|[a]	Kreisel *et al.*[52]	Symmetry	Assignment
$4f_1(\downarrow)$	719.1920	719.0674	0.1245	713	A_{1g}	Tetrahedral $Fe^{(3)}$–O_4
$2b(\uparrow)$	679.8629	679.7555	0.1074	684	A_{1g}	Bipyramid $Fe^{(2)}$–O_5
$4f_2(\downarrow)$	608.6377	608.5030	0.1347	614	A_{1g}	Octahedral $Fe^{(4)}$–O_6
	523.4077	523.3130	0.0946	527	E_{2g}	
$2a(\uparrow)$	505.1866	505.9428	0.7562	512	A_{1g}	Octahedral $Fe^{(1)}$–O_6 and $Fe^{(5)}$–O_6
	463.0669	463.0624	0.0045	467	A_{1g}	
$12k(\uparrow)$	418.7701	401.6707	17.0994	417	E_{1g}	Octahedral dominated $Fe^{(5)}$–O_6
	400.0034	397.4566	2.5468	409	A_{1g}	
	346.0538	341.2250	4.8288	340	A_{1g}	Octahedral (mixed)
	331.09216	331.2500	0.15784	335	E_{2g}	
	309.3766	309.5371	0.1604	317	E_{1g}	
	274.1963	274.1141	0.0822	285	E_{1g}	

[a] Raman shift.

modes has been listed in Table 5. These results show a shift of the (**RE.SrM**) bands that occurs towards the highest frequency value (400 to 397 cm^{-1}) or lower (346.05 to 341 cm^{-1}), while the other bands were practically unaffected by doping. These differences are related to the chemical bond length. This behavior could be explained by the fact that the introduction of small quantities of larger rare earth elements results in the displacement of oxygen atoms. Effectively, the smaller Fe^{3+} ions (which are in the octahedral site) are replaced by larger Gd^{3+}, Ho^{3+} and Sm^{3+} ions, and are responsible for such variation in the lattice of the M-type strontium hexaferrite. Therefore, the shift to a higher wavenumber for the A_{1g} vibration in the site 12k could be explained by force constant changes, which provide further proof that rare earth elements reside in the 12k site.[54] The peak frequency values observed in the spectra were compared with those in the literature for single crystals,[52] nanoparticles[55] and polycrystalline.[56] It has been noted that they are in very good agreement with those associated with single crystals and nanoparticles. All of these results are in perfect agreement with those found in the case of XRD and FTIR.

3.4. Morphological study

The morphology of the undoped and doped M-type Sr hexaferrite samples were observed by scanning electron microscopy (SEM), as shown in Fig. 8. The SEM analysis of (**SrM**) and (**RE.SrM**) indicates that the morphology is characterized by the largest grains with irregular grain shape. The configuration is almost platelet-shaped and agglomerated due to the magnetic interaction. The analysis of EDX is given in Fig. 9, and shows the presence of Sr, Fe, O, Gd, Ho and Sm in the samples. No other traceable impurities are found within the resolution limit of EDX. The small amount of carbon is related to the sample carrier of the equipment. The theoretical composition percentages of the elements were calculated using the following formula:

$$x\% = z\frac{M_s}{M_T} \times 100 \quad (2)$$

where M_s is the molar mass of the element, M_T is the total molar mass and z refers to the number of elements. The theoretical and experimental composition percentages of the elements of

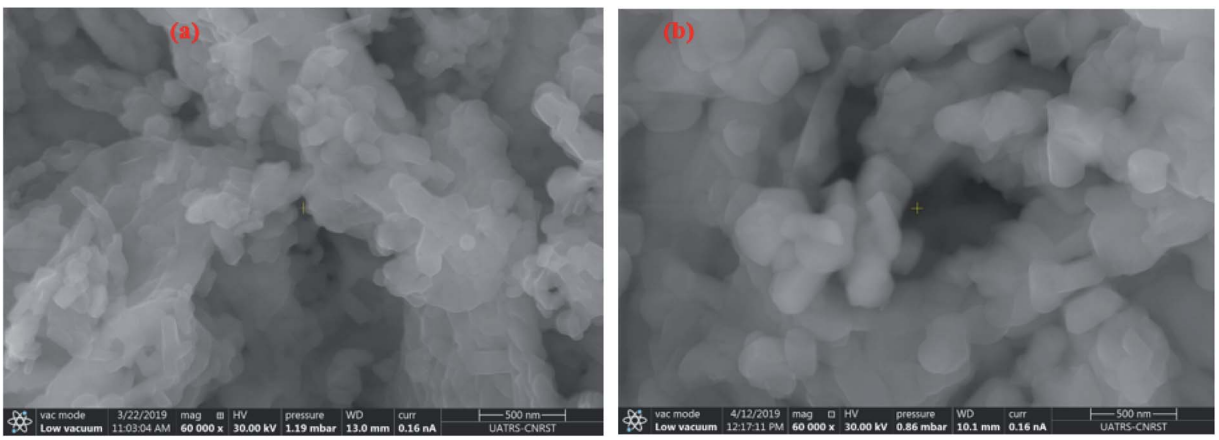

Fig. 8 SEM images and particle size distribution analysis for M-type Sr hexaferrite: (a) (**SrM**), (b) (**RE.SrM**).

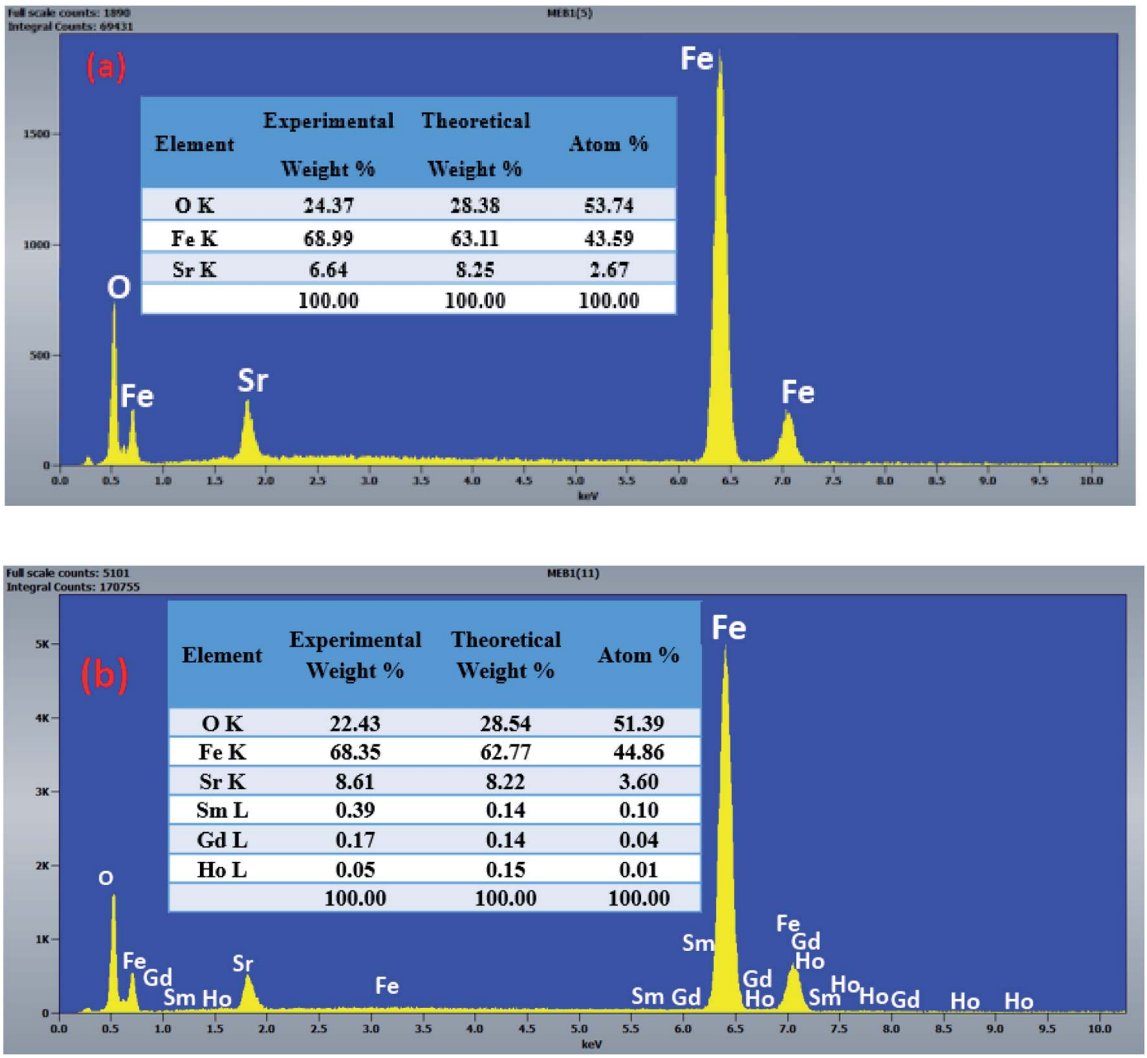

Fig. 9 EDX image analysis for M-type Sr hexaferrite: (a) (SrM), (b) (RE.SrM).

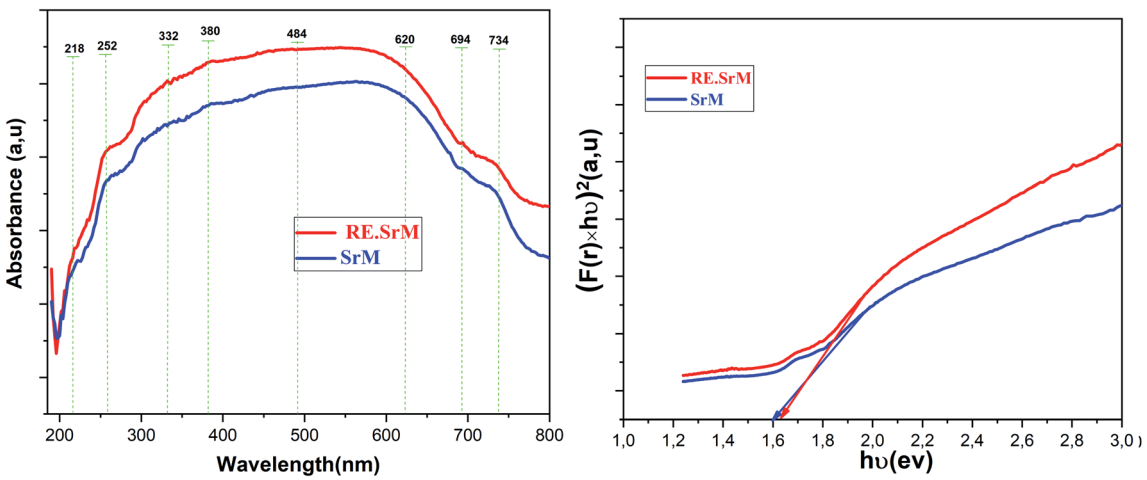

Fig. 10 Absorption spectra and optical band gap for (SrM) and (RE.SrM).

the compound are presented in Fig. 9. The experimental percentage of the element is in agreement with the theoretical values. In fact, the crystal structure showed a homogeneous chemical composition.

3.5. Optical measurements

The UV-Vis spectra of (**SrM**) and (**RE.SrM**) are shown in Fig. 10. UV-Vis analysis was performed at room temperature in the range of 190–800 nm. The absorption spectra of two samples were divided into three portions as one having the wavelength (λ) region of 190 nm < λ < 332 nm, the second region being 332 nm < λ < 620 nm, and the last region being 620 nm < λ < 800 nm. Less absorbance was observed when the value of E_g was larger than the photon energy because photons having less energy could not excite the valence electrons to move into the conduction band. Conversely, the photons having enough energy equivalent to E_g can enhance the absorbance trend. The majority of the electrons close to the valence band are absorbed by the photons within the energy range of 332 nm < λ < 620 nm. These electrons achieve enough energy from the photons, and then jump into the conduction band, causing an increase in the absorbance of photons. It implies that the absorbance occurs in the visible regime. In the case of the interval 620 nm < λ < 800 nm, the photonic energy is greater than the band gap. The absorption tends to the state of saturation, and consequently, no increase in the absorbance will take place.

The optical band gap (E_g) may be evaluated based on the optical absorption spectrum using the Kubelka–Munk (K–M) method.[57] According to the Kubelka–Munk (K–M) theory, the $[F(R) \times h\nu]^n$ *versus* ($h\nu$) curves (where $F(R) = \alpha$ is the Kubelka–Munk (K–M) function, ($h\nu$) is the photon energy) can be used to calculate the absorbed band gap energy using the following relation:

$$(\alpha h\nu) = A(h\nu - E_g)^{1/2} \quad (3)$$

where E is the energy band gap, A is a constant, and n depends on the type of electronic transition, which assumes the values of 1/2, 3/2, 2, and 3, depending on the nature of the electronic transition, and $n = 1/2$ for the direct band gap semiconductors. The optical band gap for the absorption peak was obtained by extrapolating the linear portion of the $[\alpha \times h\nu]^{1/2}$ curve *versus* ($h\nu$) to zero (Fig. 10). The optical band gap values of (**SrM**) and (**RE.SrM**), concluded from the graph, are: 1.60 eV and 1.62 eV, respectively. The lowering of the E_g values can be attributed to the crystalline size and lattice strain. This indicates that both samples are semiconductors. The E_g observed for (**RE.SrM**) is higher than that for (**SrM**). According to the literature, the variation of the optical band gap relies on factors, such as the quantum confinement and crystallite size.[58] From this work, it is possible to confirm the importance of the synthesis method, and the experimental conditions play a crucial role in determining the optical properties. For example, the $SrCo_{0.1}Fe_{11.9}O_{19}$ obtained by the sol–gel method has crystallite sizes between 12 and 14 nm, indicating an optical band gap values of 1.78 eV,[59] while the optical band gap value of the $SrFe_{12}O_{19}$ with the particle sizes of about 35 nm is 2.62 eV.[60] The pure hexaferrite obtained by co-precipitation assisted ceramic route method, with a crystallite size of 77 nm, indicate an optical band gap value of 1.74 eV.[61]

3.6. Magnetic measurements

In this section, we attempt to elucidate the effect of doping the M-type strontium hexaferrite nanoparticles, with Sm^{3+}, Gd^{3+} and Ho^{3+} ions, on the saturation magnetization M_s, coercive field H_c, remanent magnetization M_r and the energy product $(BH)_{max}$.

Fig. 11 shows the hysteresis loops of the **RE.SrM** sample at room temperature (300 K), and the applied magnetic field is ±10 kOe. Due to the absence of magnetic saturation, the saturation magnetization (M_s) of the sample could be determined using the law of approach to saturation (LAS)[62] by the following eqn (4):

$$M = M_s\left(1 - \frac{A}{H} - \frac{C}{H^2}\right) + \chi H \quad (4)$$

where M is the magnetization, A is the inhomogeneity parameter, χ is the high field susceptibility, H is the applied field and C is the anisotropy parameter. For hexagonal ferrites, C can be expressed by eqn (5):

$$C = \frac{8{K_1}^2}{105{M_s}^2} \quad (5)$$

where K_1 is the magnetocrystalline anisotropy constant. Moreover, the values of A/H and χ in eqn (4) are negligible for hexaferrite at sufficiently high magnetic fields, as explained by Néel[63] and Brown.[64] Thus, eqn (4) can be written as in eqn (6):

$$M = M_s\left(1 - \frac{8{K_1}^2}{105{M_s}^2H^2}\right) \quad (6)$$

To calculate M_s and K_1, the M–H curve data (Fig. 13) at the high external field were fitted with eqn (6). The fitted curve for the

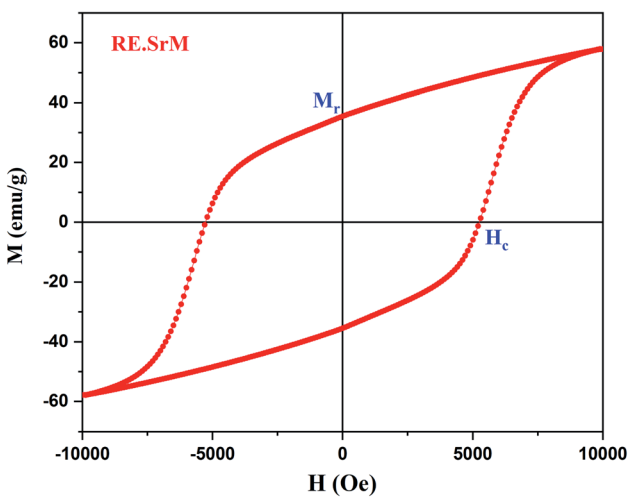

Fig. 11 Hysteresis loops of (**RE.SrM**).

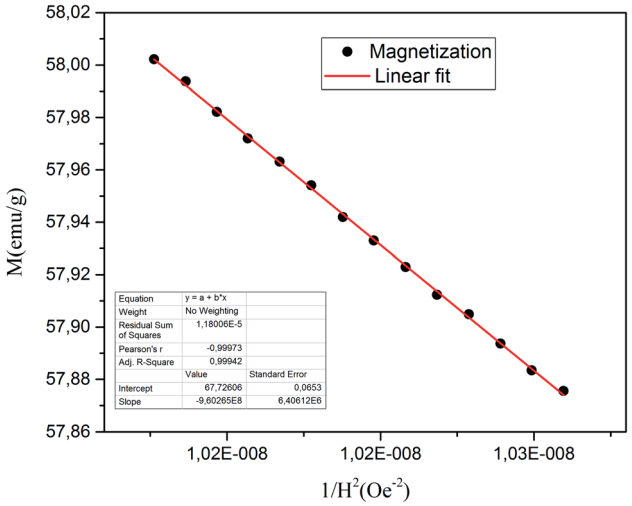

Fig. 12 *M vs.* $1/H^2$ curve for the (**RE.SrM**) sample.

(**RE.SrM**) sample is depicted in Fig. 12. Using the values of M_s and K_1, the anisotropy field H_a can be calculated using eqn (7):

$$H_a = \frac{2K_1}{M_s} \tag{7}$$

The values of M_s and M_r for the (**RE.SrM**) sample are respectively 67.72 emu g^{-1} and 35.65 emu g^{-1}. These values are significantly greater than those of the undoped strontium hexaferrite, as well as some doped strontium hexaferrites reported in the literature, as shown in Table 7. This can be explained by the following: according to Raman analysis, Gd^{3+} and Ho^{3+} ions prefer to occupy the 12k(↑) site, whereas Sm^{3+} ions prefer to occupy the 2a(↑) site. The substitution of Fe^{3+} ions in the 12k(↑) and 2a(↑) octahedral sites with Sm^{3+}, Gd^{3+}, and Ho^{3+} ions, is responsible for the increased values of M_s and M_r of the (**RE.SrM**) sample. Indeed, the theoretical magnetic moments of Gd^{3+} and Ho^{3+} ions are calculated to be 7 and 10 μ_B, respectively. These values are collectively higher than 5 μ_B, which is the value of the magnetic moment of the Fe^{3+} ion.

The theoretical total magnetic moment per unit cell of the (**RE.SrM**) compound $M_{th,tot}$(**RE.SrM**) can be calculated using eqn (8), where $M(\uparrow)$ and $M(\downarrow)$ are the magnetic moments of sublattices with spin up and spin down, respectively. $M_{th,tot}$(**RE.SrM**) can be calculated as follows:

$$\begin{aligned} M_{th,tot}(\mathbf{RE.SrM}) = 2 \times (&5.98 \times M(Fe^{3+},12k(\uparrow)) + 0.01 \\ &\times M(Gd^{3+},12k(\uparrow)) + 0.01 \times M(Ho^{3+},12k(\uparrow)) \\ &+ 0.99 \times M(Fe^{3+},2a(\uparrow)) + 0.01 \\ &\times M(Sm^{3+},2a(\uparrow)) + M(Fe^{3+},2b(\uparrow)) \\ &- M(Fe^{3+},4f_1(\downarrow)) - M(Fe^{3+},4f_2(\downarrow))) \end{aligned} \tag{8}$$

$$\begin{aligned} M_{th,tot}(\mathbf{RE.SrM}) = 2 \times ((5.98 \times 5\ \mu_B) &+ (0.01 \times (7 + 10)) \\ &+ (0.99 \times 5\ \mu_B) + (0.01 \times 0.71) + (1 \times 5\ \mu_B) \\ &- (2 \times 5\ \mu_B) - (2 \times 5\ \mu_B)) \end{aligned}$$

$$M_{th,tot}(\mathbf{RE.SrM}) = 40.043\ \mu_B \text{ per unit cell}$$

The value of the theoretical total magnetic moment per unit cell of the undoped (**SrM**) compound $M_{th,tot}$(**SrM**) can be calculated in the same manner to be 40 μ_B. Clearly, the value of $M_{th,tot}$(**RE.SrM**) is higher than that of $M_{th,tot}$(**SrM**) by 0.11%, explaining the increase in the M_s value. The experimental values of the total magnetic moment per formula unit of the (**RE.SrM**) compound M_{tot}(**RE.SrM**) can be calculated using eqn (9):[76]

$$M_{tot}(\mathbf{RE.SrM}) = \frac{M(\mathbf{RE.SrM}) \times M_s}{5585} \tag{9}$$

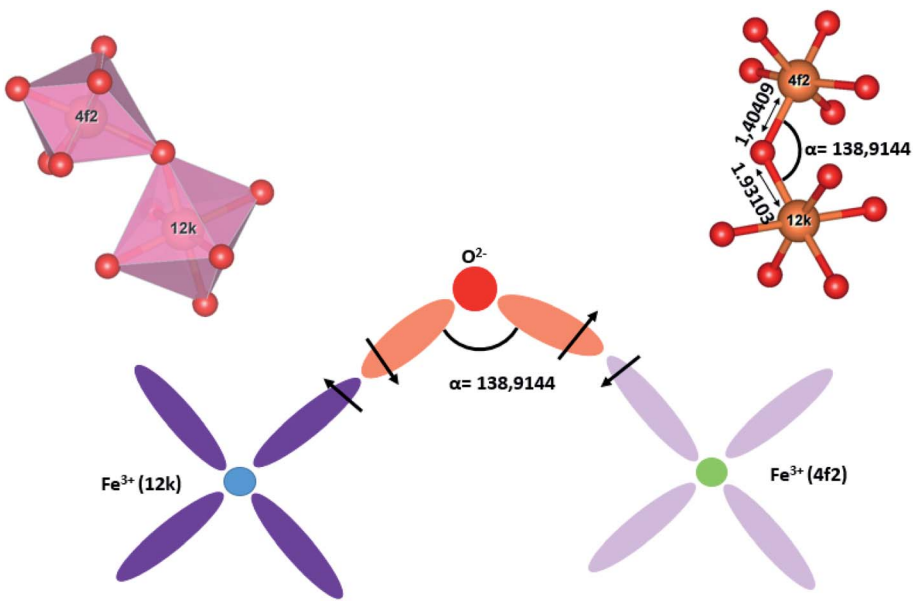

Fig. 13 Schematic diagram of the magnetic super-exchange interactions between the 12k and the $4f_2$ sites.

where M(**RE.SrM**) is the molecular weight of the (**RE.SrM**) sample, and M_s is the measured saturation magnetization at 300 K. The calculated value of M_{tot}(**RE.SrM**) per formula unit (f.u.) is 12.911 μ_B per f.u., and per unit cell is 25.822 μ_B per unit cell (at 300 K). The value of M_{tot}(**RE.SrM**) measured at 300 K is smaller than that of $M_{th,tot}$(**RE.SrM**) calculated at 0 K because of the influence of the thermal agitation on the magnetic moments.

The improvement of the coercive force ($H_c = 5257.63$ Oe) can be explained by the magnetocrystalline anisotropy and the exchange interactions. Indeed, the H_c is directly proportional to the anisotropy H_a, while H_a is also directly proportional to the magnetocrystalline anisotropy constant K_1. Therefore, H_c is directly proportional to K_1. The determined values of H_a and K_1 are respectively 22.45 10^4 Oe and 7.602 10^6 emu Oe g^{-1}. These values are improved compared with other works on doped strontium hexaferrite ($H_a = 1.9053\ 10^4$, $K_1 = 0.5558\ 10^6$ emu Oe g^{-1}).[77] In addition, the spin-orbital coupling is generally stronger in rare-earth ions than in 3d transition metal ions. Therefore, the substitution of Fe^{3+} ions with Sm^{3+} and Ho^{3+} ions improves the value of coercivity.

The crystal field perturbation effects on the 4f electrons of rare-earth ions are weak because the 4f electrons are shelled by the 5s and 5p electrons. Consequently, there are less quenching effects in rare-earth ions in comparison to 3d transition metal ions; thus, strong spin–orbit interactions occur. Doping with small amounts of Gd^{3+}, Ho^{3+}, and Sm^{3+} increases the value of the coercive field of the (**RE.SrM**) compound. Indeed, the Ho^{3+} and Sm^{3+} ions have a large anisotropy to a single ion; thus, they contribute to the anisotropy of (**RE.SrM**). However, it has been reported in the literature that Gd strengthens and contributes to anisotropy.[78]

Furthermore, it is necessary to consider the exchange interactions in the (**RE.SrM**) compound. Super-exchange is the coupling between two magnetic cations that are separated by an oxygen anion (non-magnetic). It depends on the distance of these cations from the oxygen anion through which the interactions occur, and the angle between these cations. The super-exchange interaction energy is maximum when the angle between the cations is about 180°. Moreover, the interaction energy decreases rapidly with increasing distance between the cations and the oxygen anion. This effect becomes negligible over a distance higher than 3 Å, as suggested by Anderson.[79] To study the effect of the super-exchange interaction, we calculated the respective bond lengths and bond angles, as shown in Table 2. All bond lengths in **SrM** and (**RE.SrM**) are less than 3 Å, indicating that the super-exchange interactions are non-negligible. The average bond length of the different polyhedrons ranging from largest to smallest are: octahedral > tetrahedral > bipyramidal for the (**SrM**) structure, and bipyramidal > octahedral > tetrahedral, for the (**RE.SrM**) structure.

We consider the following sub-lattice interactions: (2a(↑)–$4f_1$(↓)), (2a(↑)–12k(↑)), (2b(↑)–$4f_2$(↓)), (2b(↑)–12k(↑)), ($4f_2$(↓)–12k(↑)), ($4f_1$(↓)–12k(↑)), ($4f_2$(↓)–$4f_2$(↓)) and (12k(↑)–12k(↑)). From the values of Table 2, it can be seen that the interaction ($4f_2$(↓)–12k(↑)) is the strongest. Indeed, the $4f_2$(↓) and 12k(↑) sites have the shortest Fe–O average bond length and the largest angle value between the cations, as depicted in Fig. 13. On the other hand, the sub-lattice interaction (12k(↑)–12k(↑)) is the weakest because the 12k(↑) site has the longest Fe–O average bond length and the smallest angle value between the cations. These interactions could affect the coercive force in the following manner: during the hysteresis loops measurement of the (**RE.SrM**) sample, the magnetic moments get aligned in the direction of the external magnetic field when the external field is applied to the sample. As the external field decreases slowly, these magnetic moments have a low tendency to return to their initial positions due to the strong interactions between the magnetic moments, especially the 12k(↑) and $4f_2$(↓) sites. This could explain the high coercive force of the (**RE.SrM**) sample.

The squareness ratio (M_r/M_s) for (**RE.SrM**) has also been calculated to be 0.52. The obtained value is above the theoretical value of 0.5, indicating that the materials are a single magnetic domain. A value below 0.5 is related to the multi magnetic domains.[48] In the present work, the observed M_r/M_s value is very close to 0.5, suggesting that the synthesized sample is in the single magnetic domain.

According to the particle sizes calculated in the DRX section, the decrease of particle sizes after doping with rare earth elements is probably another reason for the improved coercivity (H_c). (H_c) has been significantly affected by particle morphology and varies inversely with grain size. With larger grain size, fewer grain boundaries will act as pinning sites for the magnetic domain wall movement. With Sm^{3+}, Gd^{3+} and Ho^{3+} doping, the grain size became smaller, and the results are consistent with XRD analysis. The reverse magnetic field for the demagnetization of the nanoparticles can be interpreted in relation with the domain rotation, where the smaller grain sizes have less domain wall movement. Consequently, the high coercivity is expected for smaller particle sizes.

To test the material's material quality for magnetic water treatment applications, the curves B–H and J–H were drawn using the equation: $B = H + 4\pi M$ in the CGS units with $J = 4\pi M$. The J–H curve is the hysteresis loop shown in Fig. 14. Two different coercivities are normally used to characterize the hardness of the permanent magnetic material, namely, the normal coercivity H_{cB} (the strength of the inverse field required

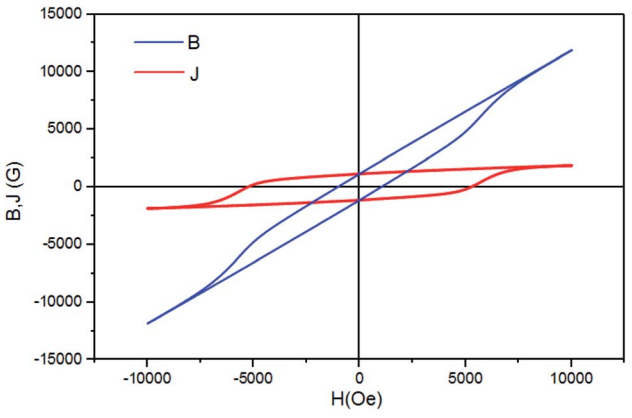

Fig. 14 B–H and J–H curves of the (**RE.SrM**) sample.

Table 6 Measured magnetic properties of the **RE.SrM** sample

H_c (Oe)	M_s (emu g^{-1})	M_r (emu g^{-1})	M_r/M_s	H_{cJ} (Oe)	H_{cB} (Oe)	K_1 (emu Oe g^{-1}) $\times 10^6$	H_a (Oe) $\times 10^4$	$(BH)_{max}$ (MGOe)	$(BH)_{max}$ (kJ m^{-3})
5258.63	67.72	35.65	0.52	5244.92	1030.45	7.602	22.45	1.06	8.46

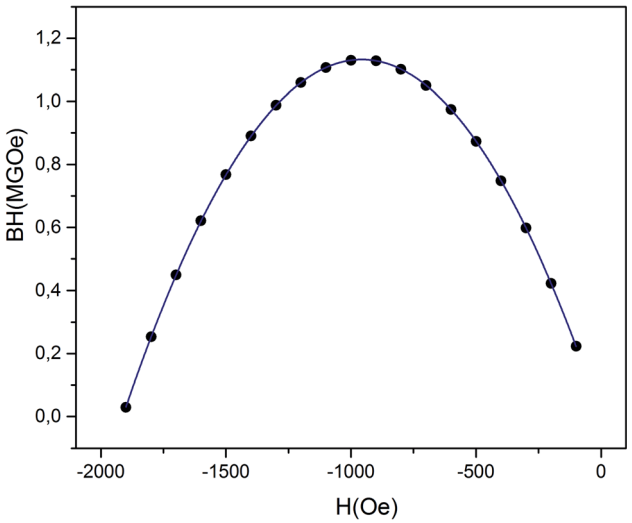

Fig. 15 Energy density *versus* reverse field in the second quadrant for the (**RE.SrM**) sample.

to reduce the *B*-induction to zero) and the intrinsic coercivity H_{cJ} (the strength of the field required to reduce the intrinsic induction $4\pi M$ to zero). A high-performance magnet is characterized by a high saturation magnetization and a high coercivity, with the intrinsic coercivity being generally much higher than the normal coercivity (H_{cB}) that is necessary for the stable operation of the magnet.

The two coercivity parameters were directly determined from the *B*–*H* and *J*–*H* curves presented in Fig. 14. The results, presented in Table 6, show that both H_{cB} and H_{cJ} increase with the substitution with the rare earth elements Gd^{3+}, Ho^{3+} and Sm^{3+}. This constitutes an improvement in the magnetic properties for permanent magnet applications, compared to other works, in particular $Sr_{0.7}La_{0.3}Fe_{11.8}Zn_{0.2}O_{19}$ (H_{cJ} = 2530.86 Oe and H_{cB} = 2459.23 Oe).[80]

From the *M*–*H* data (Fig. 11), we could also calculate the energy product $(BH)_{max}$, which is a significant factor for rating the performance of a permanent magnet. $(BH)_{max}$ is also known as a figure of merit for hard magnetic materials, and is often used to indicate their grade. Fig. 15 shows |BH| *versus H* dependences (in absolute values) of the (**RE.SrM**) sample. It can be seen that the data form a parabola in which the vertex corresponds to $(BH)_{max}$. The value of $(BH)_{max}$ is found to be 1.064 MGOe. This value is improved due to the increase in the H_c and M_r values. The reported $(BH)_{max}$ values from the literature include: 1.04 MGOe ($SrFe_{12}O_{19}$),[81] 0.363 MGOe ($Ba_{0.5}Sr_{0.5}Fe_{12}O_{19}$),[82] 0.007 MGOe ($Ba_{0.5}Sr_{0.5}Fe_{12}O_{19}$),[83] 0.9 MGOe ($SrFe_{12}O_{19}$),[84] 0.791 MGOe ($BaCoFe_{11}O_{19}$),[85] 0.96 MGOe ($BaFe_{12}O_{19}$),[86] 0.622 MGOe ($BaCr_{0.3}Ga_{0.3}Fe_{11.4}O_{19}$),[87], (0.42–0.61) MGOe ($SrFe_{12}O_{19}$),[88] 1.02 MGOe ($SrFe_{12}O_{19}$),[89] and 1.039 MGOe ($SrLa_{0.1}Fe_{11.9}O_{19}$).[90] The obtained value of $(BH)_{max}$ in this work has yielded much higher values than those reported by other researchers, which is the essential achievement of this work.

The magnetization *M* of the (**RE.SrM**) sample was measured by varying temperature *T* from 25 °C to 580 °C, as shown in Fig. 16. It can be seen that *M* decreases with increasing *T*. As the temperature increases from 25 °C, the magnetization value gradually decreases to a critical temperature after which a sudden increase in the magnetization *M* is observed. This temperature is called the blocking temperature T_B, and its value is found to be T_B = 749 K. This behavior indicates that, below the blocking temperature T_B, the (**RE.SrM**) nanoparticles are magnetically stable, and a superparamagnetic relaxation takes place when the temperature overcomes the T_B value. Moreover, it is clear that the measured magnetization shows a typical behavior. This phenomenon is called the Hopkinson effect, and the maximum just below the Curie temperature is called the Hopkinson peak. The drastic increase in magnetization can be explained by a concurrent phenomenon of thermomagnetic randomization and magnetic reorganization by the expansion of the domain boundary expansion with increasing thermal energy.[91] The relative intensity of the Hopkinson peak indicates that the (**RE.SrM**) nanoparticles are in the single-domain state, which is in good agreement with the mentioned value of the M_r/M_s ratio. In addition, a superparamagnetic relaxation occurs, resulting in a sharp peak (peak temperature) at T_{pk} = 760 K, which is below to the Curie temperature T_c = 765 K. This suggests a transition of the (**RE.SrM**) nanoparticles from a ferrimagnetic to a paramagnetic state.

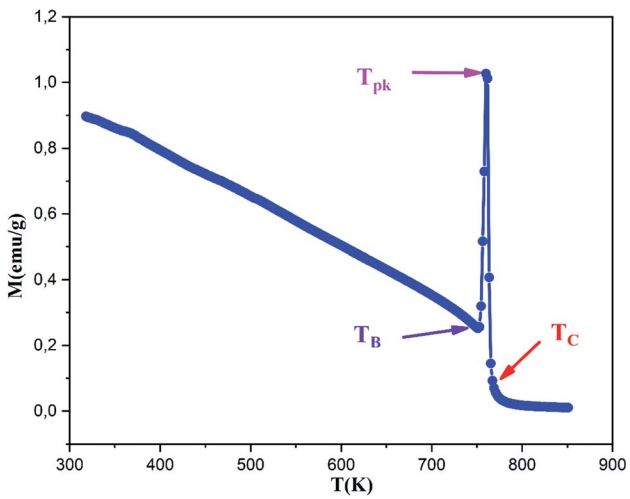

Fig. 16 Magnetization as a function of temperature (**RE.SrM**).

The value of T_c is relatively high when compared to previous works. The reported T_c values from the literature include: 737 K for ($SrFe_{12}O_{19}$),[92] 740.15 K for ($Sr_{0.95}Sm_{0.05}Fe_{12}O_{19}$)[54] and 738.15 K ($Ba_{0.5}Sr_{0.5}Fe_{11.6}Co_{0.2}(MgZn)_{0.1}O_{19}$).[93]

As the Curie temperature T_c depends on the overall strength of the exchange interactions, it can be argued that the increase of the exchange interaction energy is responsible for the increase in the T_c value. As it was already discussed, the increase in the exchange interaction energies in the compound is due to the presence of rare earth elements having a strong spin–orbit coupling and large magnetic moments, especially the Ho^{3+} ion. Indeed, to offset the effects of the exchange interactions (RE–O–Fe^{3+} and Fe^{3+}–O–Fe^{3+}) in the (**RE.SrM**) compound, a greater amount of energy will be required.

3.7. *Ab initio* study

3.7.1. Site preference study. To gain insight into the effects of doping the M-type strontium hexaferrite with the rare-earth elements Sm, Gd and Ho on its structural, electronic and magnetic properties from a theoretical perspective, first-principles calculations were conducted on the different configurations of $SrFe_{12-x}X_xO_{19}$ with $x = 0$, 0.5 and X = Sm, Gd, Ho.

The magnetic properties of the strontium hexaferrite can be adjusted by substituting Fe atoms with other atoms, such as rare earth elements. The Fe atoms occupy five distinct crystallographic sites, namely, the 2a, 2b, $4f_1$, $4f_2$ and 12k sites. The substitution of Fe atoms with other elements give rise to energetically distinct configurations (denoted [X,s] with element X in the site s). To complement the present XRD and Raman spectroscopy results, a site preference study was conducted for the substituting elements Sm, Gd and Ho. This can be

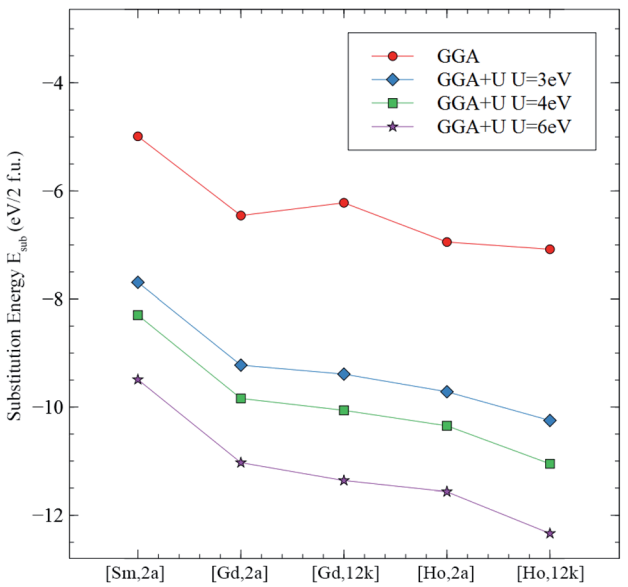

Fig. 17 Substitution energies E_{sub} for the studied configurations calculated using the GGA and the GGA+U methods with $U_{eff} = 3$, 4 and 6 eV.

Table 7 Magnetic properties of undoped and doped $SrFe_{12}O_{19}$ prepared by different synthesis methods

	Phase	pH	Calcination temperature (°C)	Duration of calcination	Crystallite size (nm)	Magnetic parametres				Ref.
						Applied field (KOe)	M_s (emu g^{-1})	M_r (emu g^{-1})	H_c (Oe)	
Sol–gel	Undoped $SrFe_{12}O_{19}$	7	1100	5 h	45.15	±13	46.9	34	46.9	65
	$SrGd_{0.01}Sm_{0.01}Ho_{0.01}Fe_{11.97}O_{19}$	7	1000	—	49.85	±10	67.72	35.65	5257.63	Present work
	$Sr_{0.975}$ $Ce_{0.025}Fe_{11.75}Mn_{0.25}O_{19}$	7–8	950	8 h	1782	±10	59.80	17.30	256.09	66
	$SrAl_4La_{0.5}Sm_{0.5}Fe_7O_{19}$	7–8	1100	1 h	43.80	±10	53.271	22.313	623.286	67
	$Sr_{0.5}Cu_{0.2}Mg_{0.3}Fe_{12}O_{19}$	7–8	1200	4 h	2120	±10	72.55	45.29	1987.40	68
	$Ba_{0.4}Sr_{0.6}Al_{0.3}$ $Sm_{0.1}Fe_{11.09}O_{19}$	—	1000	1 h 30	—	±10	42.73	25.48	2700	69
	$Sr(NdLa)_{0.4}Fe_{11.2}O_{19}$	6.5	900	10 h	30.62	—	47.7	—	6308	45
Co-precipitation	$Sr_{0.5}Ba_{0.98}Pr_{0.02}Fe_{11.80}Ni_{0.2}O_{19}$	9	1050	6 h	41	±7	—	—	2790	70
	$Sr_{0.85}Sm_{0.15}Fe_{11.85}Cu_{0.15}O_{19}$	7	800	2 h	—	±12	59.96	—	6862	71
	$Sr(CeNd)_{0.25}Fe_{11.5}O_{19}$	13	900	2 h	29	±15	52.36	30.90	5010	72
Solid state	$Sr_{0.7}La_{0.1}Ce_{0.2}Fe_{11.7}Zn_{0.3}O_{19}$	—	1200	2 h	—	±5	67.2	—	2685	73
	$Ca_{0.4}Sr_{0.44}Gd_{0.16}Fe_{11.84}O_{19}$	—	1185	1 h 5	51.97	±20	63.80	26.44	1332.7	74
	$Ca_{0.4}Sr_{0.44}Nd_{0.16}Fe_{11.84}(NbZn)_{0.08}O_{19}$	—	1625	2 h	48.2	±30	60.915	17.359	617.7	75

Table 8 Calculated properties of the pristine and doped strontium hexaferrite $SrFe_{12-x}X_xO_{19}$ with $x = 0$, 0.5 and X = Sm, Gd, Ho: substitution energies E_{sub} of the [X,s] configuration with the element X in the site s (in eV) using the GGA+U method ($U = 3$ eV), the multiplicity g, the total magnetic moment M_{tot} of the unit cell containing 2 formula units (*i.e.*, 64 atoms) in Bohr magneton (μ_B), the volume of the unit cell V (in Å^3), the lattice parameters a, b, c, α, β and γ (in degrees °)

Configuration	E_{sub} (eV)	G	M_{tot} (μ_B)	a (Å)	b (Å)	c (Å)	V (Å^3)	α (°)	β (°)	γ (°)
$SrFe_{12}O_{19}$	—	—	40.02	5.8259	5.8259	22.9161	673.59	90	90	120
[Sm,2a]	−7.693	2	40.00	5.8533	5.8533	23.3461	692.71	90	90	120
[Gd,2a]	−9.223	2	41.99	5.8529	5.8529	23.3077	691.47	90	90	120
[Gd,12k]	−9.389	12	42.00	5.8579	5.9126	23.1089	695.27	90.19	90	119.69
[Ho,2a]	−9.716	2	31.01	5.8521	5.8521	23.2607	689.89	90	90	120
[Ho,12k]	−10.248	12	38.96	5.8596	5.9034	23.0936	693.51	90.19	90	119.75

Table 9 Calculated properties of the pristine and doped strontium hexaferrite $SrFe_{12-x}X_xO_{19}$ with $x = 0$, 0.5 and X = Sm, Gd, Ho: the spin magnetic moment of the Fe LAPW spheres M(Fe) in the sites 2a, 2b, $4f_1$, $4f_2$ and 12k in Bohr magneton, the spin magnetic moment of the doping elements M(X) with X = Sm, Gd, Ho in the 2a and 12k sites in Bohr magneton, the total magnetic moment M_{tot} of the unit cell containing 2 formula units (*i.e.*, 64 atoms) in Bohr magneton (μ_B)

	M(Fe) (μ_B) in:					M(X) (μ_B) X = Sm, Gd, Ho in:		
Configuration	2a	2b	$4f_1$	$4f_2$	12k	2a	12k	M_{tot} (μ_B)
$SrFe_{12}O_{19}$	3.93	3.83	−3.83	−3.91	3.98	—	—	40.02
[Sm,2a]	3.98	3.84	−3.80	−3.85	3.96	4.89	—	40.00
[Gd,2a]	3.98	3.85	−3.81	−3.86	3.96	6.81	—	41.99
[Gd,12k]	3.97	3.85	−3.81	−3.87	3.96	—	6.81	42
[Ho,2a]	3.98	3.85	−3.81	−3.86	3.96	3.8	—	38.98
[Ho,12k]	3.98	3.85	−3.81	−3.87	3.96	—	3.9	38.96

accomplished by calculating the substitution energy E_{sub}[X,s] of the element X in the site s using eqn (10):

$$E_{sub}[X,s] = E_{SrFeXO}[s] - E_{SrFeO} + E_{Fe} - E_X \quad (10)$$

where E_{SrFeXO}[s] is the total energy per unit cell (64 atoms) of strontium hexaferrite substituted with the X element in the s site, whereas E_{SrFeO} is the total energy per unit cell of pristine strontium hexaferrite. E_{Fe} and E_X are respectively the total energy per atom for Fe and X atoms (X = Sm, Gd, Ho) in their most stable crystal structure. The results from the present XRD and Raman spectroscopy work indicate that Ho^{3+}, Sm^{3+} and Gd^{3+} are occupying the octahedral sites 12k and 2a in the (**RE.SrM**) material. Therefore, we attempt to investigate the site preference of these rare earth elements in the octahedral sites, (2a), ($4f_2$) and (12k), by calculating their respective substitution energy. We also include the $4f_2$ site in this study.

Some of the calculations that were conducted have not converged, namely, the calculations for the structure optimization of strontium hexaferrite substituted with Sm in the $4f_2$ and 12k sites, and both Gd and Ho in the ($4f_2$) site. This indicates that these configurations are more likely to be unstable; therefore, they were omitted from the present site preference study. Consequently, the configurations to be investigated are the following:

[Sm,2a], [Gd,2a], [Gd,12k], [Ho,2a] and [Ho,12k]

Fig. 17 shows the graph corresponding to the calculated substitution energy E_{sub} of Sm, Gd, and Ho in the octahedral sites of 2a and 12k, using the GGA and the GGA+U methods. It can be seen that the curve from the GGA method, as well as the 3 curves from GGA+U have a common trend: Sm in 2a site having the highest substitution energy, and Ho in the 12k site having the lowest value for E_{sub}. The more stable and energetically favorable substitution site corresponds to that of the lowest substitution energy. From the GGA calculations, the configurations ranging from the least stable to the most stable, are: [Sm,2a], [Gd,12k], [Gd,2a], [Ho,2a], then [Ho,12k]. However, those from the GGA+U calculations ranging from the least stable to the most stable are: [Sm,2a], [Gd,2a], [Gd,12k], [Ho,2a], then [Ho,12k]. This is consistent with the results using the GGA+U method with $U_{eff} = 3$, 4 and 6 eV.

In conclusion, from the substitution energy concerning the site preference study, the Sm^{3+} occupies the 2a site, whereas Gd^{3+} and Ho^{3+} both occupy the 12k sites. This is in very good agreement with the present XRD and Raman spectroscopy results.

3.7.2. Electronic and magnetic properties. Table 8 shows the calculated substitution energies E_{sub}[X,s] of elements X = (Sm, Gd, Ho) in the site s in eV using the GGA+U method with $U = 3$ eV, in addition to the total magnetic moment M_{tot} of the unit cell and the cell parameters. It can be seen that the greatest value for M_{tot} is for the configurations [Gd,2a] and [Gd,12k],

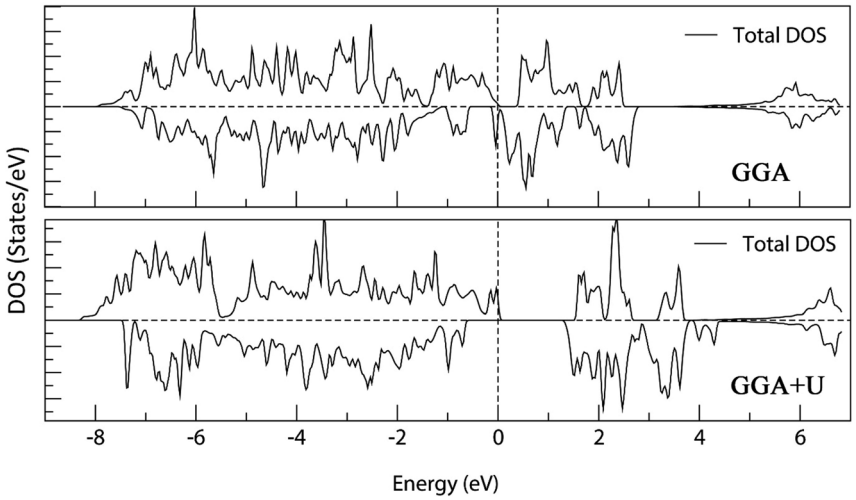

Fig. 18 Total Density Of States (DOS) of M-type strontium hexaferrite $SrFe_{12}O_{19}$ calculated using the GGA method (top); and the GGA+U method with $U_{eff} = 4$ eV (bottom). The Fermi energy is set to zero.

where the doping element is Gd. This is due to the large value of the spin magnetic moment of Gd^{3+}, calculated to be 6.81 μ_B (Table 9). The volume of the lattice gets larger by at least 2.3% upon doping with each of the rare earth elements. This can be explained by the larger ionic radius of the Sm^{3+}, Gd^{3+} and Ho^{3+} ions of 0.96, 0.94 and 1.04 Å, respectively, compared to the Fe^{3+} ions. It can be noticed that the angles remain intact upon doping in the 2a sites, but change slightly upon doping in the 12k sites. These results are not consistent with the present experimental lattice parameters for the (**RE.SrM**) structure, for which the lattice volume is smaller than that of the undoped **SrM** material. In fact, the decrease of the lattice volume upon doping with rare earth elements can be explained by the existence of the exchange interactions between the Fe^{3+} ions and the doping elements, which might overcome the effect of the electrostatic repulsion from Sm^{3+}, Gd^{3+} and Ho^{3+} ions, having larger ionic radii. These exchange interactions are not accounted for in the calculations of the structural optimization, which explains the increase of the calculated lattice volume.

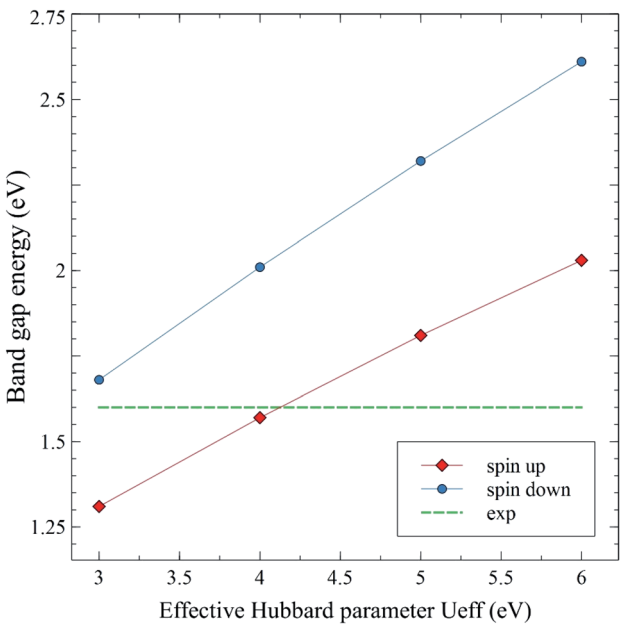

Fig. 19 Calculated spin up and spin down band gap energies of pristine $SrFe_{12}O_{19}$ using the GGA+U method with $U_{eff} = 3$, 4, 5 and 6 eV. The green dashed line represents the experimental gap energy from the UV-Vis measurements.

The band gap problem is among the issues of the GGA approximation. The calculated band gaps of semiconductors are systematically underestimated with respect to the experimental values.[94] One way to address the problem is to introduce an effective on-site Coulomb interaction term (referred to as the effective Hubbard parameter U_{eff}) to the Hohenberg–Kohn–Sham Hamiltonian. This GGA+U method corrects for the self-interaction error present in the GGA approximation, and the band gap is no longer underestimated.

Fig. 18 shows the calculated density of states of the M-type strontium hexaferrite $SrFe_{12}O_{19}$ using the GGA and the GGA+U methods with $U_{eff} = 4$ eV. It can be seen that the GGA method give rise to a metallic behavior for the structure. The band gap is clearly underestimated with the GGA method. On the other hand, the GGA+U method produces an electronic structure corresponding to a semi-conductor, as it was shown experimentally in previous works.[60,61,95–98]

Fig. 19 shows the calculated spin up and spin down band gap energies of the M-type strontium hexaferrite $SrFe_{12}O_{19}$ using the GGA+U method with $U_{eff} = 3$, 4, 5 and 6 eV, compared to the present experimental value from the optical measurements. It can be seen from the graphs that the two curves are roughly linear. The GGA+U method with $U_{eff} = 4$ eV gives rise to a band gap energy value of 1.57 eV (corresponding to the majority spin channel, *i.e.*, the spin up channel), which is in good agreement with the present experimental optical band gap of 1.60 eV. The GGA+U method with $U_{eff} = 4$ eV was used for calculating the total Density Of States (DOS) and the Partial Density Of States

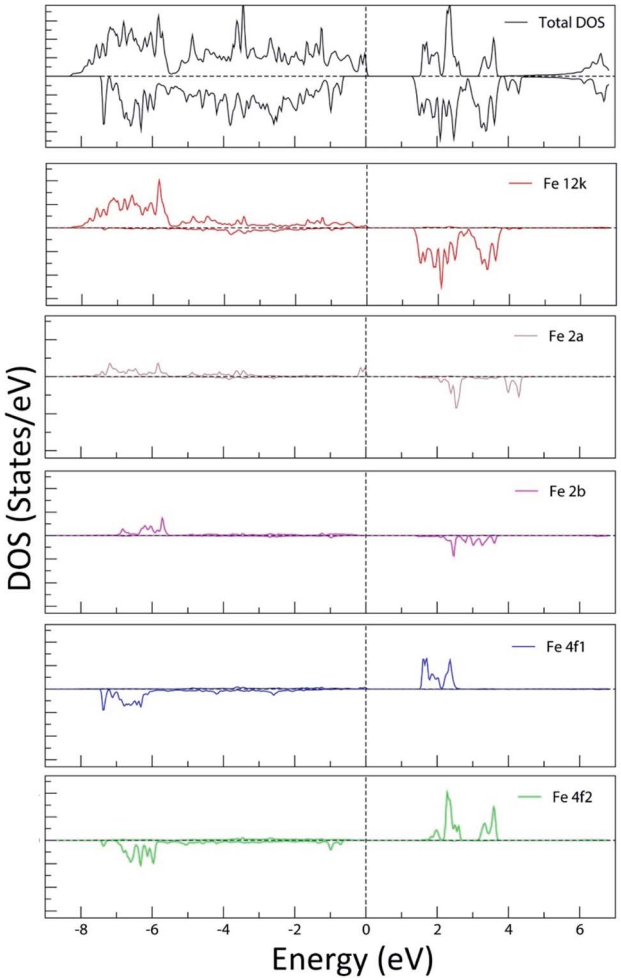

Fig. 20 Total and partial density of states (Fe LAPW spheres in 12k, 2a, 2b, $4f_1$ and $4f_2$ sites) of the M-type strontium hexaferrite $SrFe_{12}O_{19}$ calculated using the GGA+U method with U_{eff} = 4 eV. The Fermi energy is set to zero.

(PDOS) of the Fe LAPW spheres of the strontium hexaferrite $SrFe_{12}O_{19}$ (Fig. 20), as well as for calculating the DOS and the PDOS of Sm, Gd and Ho LAPW spheres of the structures $SrFe_{11.5}X_{0.5}O_{19}$ with X = Sm, Gd and Ho, respectively (Fig. 21).

In Fig. 20, the PDOS of the Fe LAPW spheres show the occupied low-lying energy Fe-3d bands, extending on average from −7.5 eV to the Fermi level. The 3d vacant bands start from the bottom of the valence band and extend to around 4.5 eV above the Fermi energy level. It can be seen that the PDOS of Fe in the octahedral sites (12k, 2a and $4f_2$) is characteristic of the electronic configuration t_{2g}^3 e_g^2 of the high spin state of the octahedrally coordinated Fe^{3+}. The crystal field separation of the vacant t_{2g} and e_g bands is clearly observed. In addition, it can be shown that the PDOS of the tetrahedrally coordinated Fe in the $4f_1$ site is characteristic of the electronic configuration e^2 t_2^3 of the high spin state of the tetrahedrally coordinated Fe^{3+}. The occupied Fe-3d bands in the $4f_1$ and $4f_2$ sites are quite similar. Nevertheless, the vacant Fe-3d bands in the tetrahedral $4f_1$ site are narrower than those of Fe in the octahedral sites,

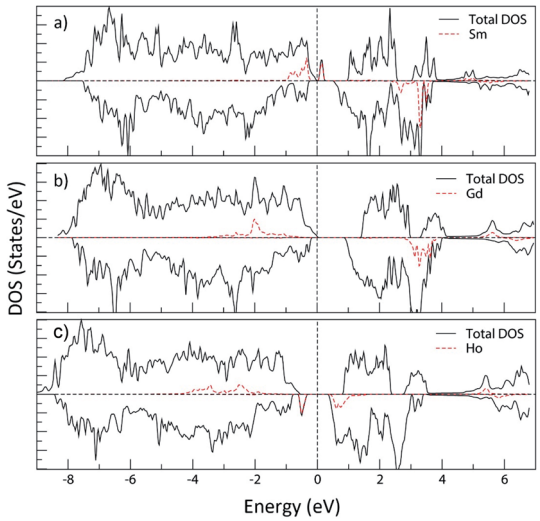

Fig. 21 Total and partial density of states (Sm, Gd and Ho LAPW spheres) of: (a) $SrFe_{11.5}Sm_{0.5}O_{19}$; (b) $SrFe_{11.5}Gd_{0.5}O_{19}$ and (c) $SrFe_{11.5}Ho_{0.5}O_{19}$; using the GGA+U method with U_{eff} = 4 eV. The Fermi energy is set to zero.

reflecting a smaller field splitting, as it is expected from the ionic crystal-field theory.

Fig. 21 shows the total and partial density of states (Sm, Gd and Ho LAPW spheres) of $SrFe_{11.5}Sm_{0.5}O_{19}$ (Sm in the 2a site), $SrFe_{11.5}Gd_{0.5}O_{19}$ (Gd in the 12k site) and $SrFe_{11.5}Ho_{0.5}O_{19}$ (Ho in the 12k site) using the GGA+U method (U_{eff} = 4 eV). It is observed that the electronic structure of strontium hexaferrite is affected, especially the band gap energy, upon doping with any of the three elements. The PDOS of the rare earth elements extending from −6 eV to 4 eV (with respect to the Fermi level) are mostly 4f states.

The density of states of $SrFe_{11.5}Sm_{0.5}O_{19}$, where Sm^{3+} ions occupy the 2a site, shows the creation of occupied bands extending from −1 eV to −0.3 eV. Additional vacant bands are created near the Fermi energy, and others in the higher energies. This is characteristic of the electronic configuration, A_{2u}^1 T_{2u}^3 T_{1u}^1, of the octahedrally coordinated Sm^{3+} (Fig. 22(a)). The band gap energy is therefore significantly reduced.

The density of states of $SrFe_{11.5}Gd_{0.5}O_{19}$, where Gd^{3+} ions occupy the 12k site, shows the creation of the low-lying energy occupied Gd 4f bands extending from −3.5 eV to −0.5 eV, where the band gap energy is weakly affected. These bands correspond to the electronic configuration, A_{2u}^1 T_{2u}^3 T_{1u}^3, of the octahedrally coordinated Gd^{3+} (Fig. 22(b)).

On the other hand, the DOS of $SrFe_{11.5}Ho_{0.5}O_{19}$, where Ho^{3+} occupy the 12k site, displays a creation of low-lying energy occupied bands in the majority spin channel extending from −4.4 eV to −1.9 eV, in addition to a narrow band in the minority spin channel, decreasing the band gap energy to 1.01 eV. These bands are characteristic of the electronic configuration A_{2g}^2 T_{2g}^5 T_{1g}^3 of the octahedrally coordinated Ho^{3+} (Fig. 22(c)).

This study suggests that the band gap would be decreased upon doping with Sm^{3+}, Gd^{3+} and Ho^{3+} ions. However, as it is seen in Section 3.5, the experimental band gap energy from the

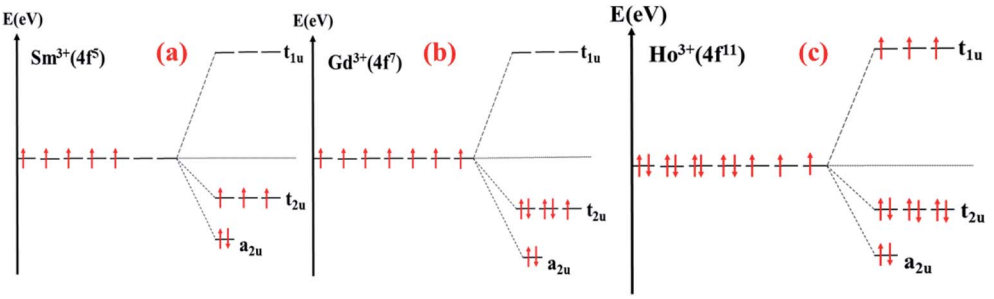

Fig. 22 Schematic diagram of the crystal field splitting of: (a) Sm^{3+}; (b) Gd^{3+}; (c) Ho^{3+} in the octahedral field.

present work is not affected upon doping. It is measured to be 1.60 eV for the **SrM** compound and 1.62 eV for the (**RE.SrM**) compound.

4. Conclusion

In the present work, the sol–gel method was found to be economical and efficient for the synthesis of Gd–Ho–Sm doped M-type Sr hexaferrite nanoparticles. XRD structural analysis reveals a single-phase hexaferrite at 1000 °C. Rietveld refinement has confirmed the formation of a hexagonal structure with space group $P6_3/mmc$ and a decrease of the lattice constant. The crystallite size calculated is in the order of 49 nm. The crystallization was confirmed by FTIR spectroscopy. The Raman spectra confirm the formation of octahedral, tetrahedral and trigonal-bipyramidal sites. From the proposed cation distribution, we note that the Gd^{3+} and Ho^{3+} ions have strong preferences towards the 12k site, whereas the Sm^{3+} ions prefer to occupy the 2a site. The SEM analysis and EDS spectroscopy confirmed the morphology and homogeneous composition. The calculated band gap from the UV-Vis NIR spectroscopy spectra indicates that the sample is a semiconductor. The magnetic properties prove that (**RE.SrM**) belongs to the class of hard-magnetic materials. The substitution of the Fe^{3+} ions with Sm^{3+}, Gd^{3+}, and Ho^{3+} ions is responsible for the increased values of M_s and M_r. The improvement in H_c is due to the contribution of the magnetocrystalline anisotropy of the Gd^{3+} and Sm^{3+} ions. The improvement of $(BH)_{max}$ is due to the increase of H_c and M_r. The ferrimagnetic nature and the initial magnetization behavior illustrate the typical behavior of the single-domain particles. The temperature-dependent magnetization shows a Hopkinson peak before transition. The M_r/M_s ratio confirms the single domain nature.

First-principles calculations were conducted on $SrFe_{12-x}X_xO_{19}$ with $x = 0$, 0.5 and X = Sm, Gd, Ho to investigate the effects of doping the M-type strontium hexaferrite with the rare-earth elements Sm, Gd, and Ho on its structural, electronic and magnetic properties. The site preference study reveals that the Sm^{3+} ions preferably occupy the 2a site, whereas Gd^{3+} and Ho^{3+} ions both preferably occupy the 12k sites, which is in very good agreement with the XRD and Raman spectroscopy results in the present work. The GGA+U method gave rise to a semiconducting behavior for the doped and pristine Sr hexaferrite structure. The hard ferrimagnetism is a good magnetic response, making this material very interesting for water treatment applications.

Conflicts of interest

There are no conflicts to declare.

Acknowledgements

This research did not receive any specific grant from funding agencies in the public, commercial, or not-for-profit sectors.

References

1 W. Yongfei, L. Qiaoling, Z. Cunrui and J. Hongxia, *J. Alloys Compd.*, 2009, **467**, 284–287.
2 T. Xie, L. Xu and C. Liu, *Powder Technol.*, 2012, **232**, 87–92.
3 M. N. Ashiq, S. Shakoor, M. Najam-ul-Haq, M. F. Warsi, I. Ali and I. Shakir, *J. Magn. Magn. Mater.*, 2015, **374**, 173–178.
4 S. Chino, S. Ogasawara, T. Miura, A. Chiba, M. Takemoto and N. Hoshi, in *2011 IEEE Energy Conversion Congress and Exposition*, IEEE, Phoenix, AZ, USA, 2011, pp. 2805–2811.
5 M. Chirca, S. Breban, C. Oprea and M. M. Radulescu, in *2014 International Conference on Optimization of Electrical and Electronic Equipment (OPTIM)*, IEEE, Bran, Romania, 2014, pp. 472–476.
6 U. Surendran, O. Sandeep and E. J. Joseph, *Agric. Water Manag.*, 2016, **178**, 21–29.
7 M. C. Amiri and A. A. Dadkhah, *Colloids Surf., A*, 2006, **278**, 252–255.
8 C. Santhosh, V. Velmurugan, G. Jacob, S. K. Jeong, A. N. Grace and A. Bhatnagar, *Chem. Eng. J.*, 2016, **306**, 1116–1137.
9 P. E. Kazin, L. A. Trusov, D. D. Zaitsev, Y. D. Tretyakov and M. Jansen, *J. Magn. Magn. Mater.*, 2008, **320**, 1068–1072.
10 A. Morisako, T. Naka, K. Ito, A. Takizawa, M. Matsumoto and Y.-K. Hong, *J. Magn. Magn. Mater.*, 2002, **242–245**, 304–310.
11 M. J. Iqbal, M. N. Ashiq, P. Hernandez-Gomez and J. M. Munoz, *J. Magn. Magn. Mater.*, 2008, **320**, 881–886.
12 H. Z. Wang, B. Yao, Y. Xu, Q. He, G. H. Wen, S. W. Long, J. Fan, G. D. Li, L. Shan, B. Liu, L. N. Jiang and L. L. Gao, *J. Alloys Compd.*, 2012, **537**, 43–49.
13 L. A. Trusov, E. A. Gorbachev, V. A. Lebedev, A. E. Sleptsova, I. V. Roslyakov, E. S. Kozlyakova, A. V. Vasiliev,

R. E. Dinnebier, M. Jansen and P. E. Kazin, *Chem. Commun.*, 2018, **54**, 479–482.
14 R. C. Pullar, *Prog. Mater. Sci.*, 2012, **57**, 1191–1334.
15 G. M. Rai, M. A. Iqbal and K. T. Kubra, *J. Alloys Compd.*, 2010, **495**, 229–233.
16 P. A. Mariño-Castellanos, A. C. Moreno-Borges, G. Orozco-Melgar, J. A. García and E. Govea-Alcaide, *Phys. B*, 2011, **406**, 3130–3136.
17 M. Liu, X. Shen, F. Song, J. Xiang and X. Meng, *J. Solid State Chem.*, 2011, **184**, 871–876.
18 S. Ounnunkad and P. Winotai, *J. Magn. Magn. Mater.*, 2006, **301**, 292–300.
19 I. Bsoul and S. H. Mahmood, *J. Alloys Compd.*, 2010, **489**, 110–114.
20 G. Litsardakis, I. Manolakis, C. Serletis and K. G. Efthimiadis, *J. Magn. Magn. Mater.*, 2007, **316**, 170–173.
21 X. Liu, W. Zhong, S. Yang, Z. Yu, B. Gu and Y. Du, *Phys. Status Solidi A*, 2002, **193**, 314–319.
22 J. F. Wang, C. B. Ponton and I. R. Harris, *J. Alloys Compd.*, 2005, **403**, 104–109.
23 J. F. Wang, C. B. Ponton and I. R. Harris, *IEEE Trans. Magn.*, 2002, **38**, 2928–2930.
24 J. F. Wang, C. B. Ponton and I. R. Harris, *J. Magn. Magn. Mater.*, 2006, **298**, 122–131.
25 M. Jamalian, A. Ghasemi and E. Paimozd, *J. Electron. Mater.*, 2014, **43**, 1076–1082.
26 S. Kanagesan, M. Hashim, S. Jesurani, T. Kalaivani and I. Ismail, *Mater. Sci. Appl.*, 2014, **05**, 171–176.
27 L. Qiao, L. You, J. Zheng, L. Jiang and J. Sheng, *J. Magn. Magn. Mater.*, 2007, **318**, 74–78.
28 A. Ghasemi, A. Morisako and X. Liu, *J. Magn. Magn. Mater.*, 2008, **320**, 2300–2304.
29 H. F. Lu, R. Y. Hong and H. Z. Li, *J. Alloys Compd.*, 2011, **509**, 10127–10131.
30 X. Yang, Q. Li, J. Zhao, B. Li and Y. Wang, *J. Alloys Compd.*, 2009, **475**, 312–315.
31 J. Ding, W. F. Miao, P. G. McCormick and R. Street, *J. Alloys Compd.*, 1998, **281**, 32–36.
32 Y.-P. Fu, C.-H. Lin and K.-Y. Pan, *J. Alloys Compd.*, 2003, **349**, 228–231.
33 D.-H. Kim, Y.-K. Lee, K.-M. Kim, K.-N. Kim, S.-Y. Choi and I.-B. Shim, *J. Mater. Sci.*, 2004, **39**, 6847–6850.
34 I. Perelshtein, N. Perkas, Sh. Magdassi, T. Zioni, M. Royz, Z. Maor and A. Gedanken, *J. Nanopart. Res.*, 2008, **10**, 191–195.
35 A. Manikandan, J. J. Vijaya and L. J. Kennedy, *J. Nanosci. Nanotechnol.*, 2013, **13**, 2986–2992.
36 P. Giannozzi, S. Baroni, N. Bonini, M. Calandra, R. Car, C. Cavazzoni, D. Ceresoli, G. L. Chiarotti, M. Cococcioni, I. Dabo, A. D. Corso, S. de Gironcoli, S. Fabris, G. Fratesi, R. Gebauer, U. Gerstmann, C. Gougoussis, A. Kokalj, M. Lazzeri, L. Martin-Samos, N. Marzari, F. Mauri, R. Mazzarello, S. Paolini, A. Pasquarello, L. Paulatto, C. Sbraccia, S. Scandolo, G. Sclauzero, A. P. Seitsonen, A. Smogunov, P. Umari and R. M. Wentzcovitch, *J. Phys.: Condens. Matter*, 2009, **21**, 395502.
37 J. P. Perdew, K. Burke and M. Ernzerhof, *Phys. Rev. Lett.*, 1996, **77**, 3865.
38 H. J. Monkhorst and J. D. Pack, *Phys. Rev. B: Solid State*, 1976, **13**, 5188–5192.
39 P. Blaha, K. Schwarz, G. K. H. Madsen, D. Kvasnicka, J. Luitz, R. Laskowski, F. Tran and L. D. Marks, *WIEN2k, An Augmented Plane Wave + Local Orbitals Program for Calculating Crystal Properties*, ed. Karlheinz Schwarz, Techn. Universität Wien, Austria, 2018, ISBN 3-9501031-1-2.
40 V. I. Anisimov, J. Zaanen and O. K. Andersen, *Phys. Rev. B: Condens. Matter Mater. Phys.*, 1991, **44**, 943.
41 R. Joshi, C. Singh, J. Singh, D. Kaur, S. B. Narang and R. B. Jotania, *J. Mater. Sci.: Mater. Electron.*, 2017, **28**, 11969–11978.
42 R. S. Azis, S. Sulaiman, I. R. Ibrahim, A. Zakaria, J. Hassan, N. N. C. Muda, R. Nazlan, N. M. Saiden, Y. W. Fen, M. S. Mustaffa and K. A. Matori, *Nanoscale Res. Lett.*, 2018, **40**, 773–783.
43 T. R. Wagner, *J. Solid State Chem.*, 1998, **136**, 120–124.
44 C. Cui, L. Xu, T. Xie, C. Liu and J. Yang, *Mater. Focus*, 2014, **3**, 355–360.
45 A. Thakur, P. B. Barman and R. R. Singh, *Mater. Chem. Phys.*, 2015, **156**, 29–37.
46 V. Dimitrov and T. Komatsu, *J. Solid State Chem.*, 2002, **163**, 100–112.
47 N. Hayashi, *J. Electrochem. Soc.*, 1999, **146**, 1351.
48 Y. Mouhib, M. Belaiche and S. Briche, *Phys. Status Solidi A*, 2018, **215**, 1800469.
49 Q. Wu, Z. Yu, H. Hao, Y. Chu and H. Xie, *J. Mater. Sci.: Mater. Electron.*, 2017, **28**, 12768–12775.
50 R. S. Yadav, I. Kuřitka, J. Vilcakova, J. Havlica, L. Kalina, P. Urbánek, M. Machovsky, D. Skoda, M. Masař and M. Holek, *Ultrason. Sonochem.*, 2018, **40**, 773–783.
51 S. S. Seyyed Afghahi, R. Peymanfar, S. Javanshir, Y. Atassi and M. Jafarian, *J. Magn. Magn. Mater.*, 2017, **423**, 152–157.
52 J. Kreisel, G. Lucazeau and H. Vincent, *J. Solid State Chem.*, 1998, **137**, 127–137.
53 W. Y. Zhao, P. Wei, X. Y. Wu, W. Wang and Q. J. Zhang, *J. Appl. Phys.*, 2008, **103**, 063902.
54 M. A. P. Buzinaro, N. S. Ferreira, F. Cunha and M. A. Macêdo, *Ceram. Int.*, 2016, **42**, 5865–5872.
55 V. Anbarasu, P. M. Md Gazzali, T. Karthik, A. Manigandan and K. Sivakumar, *J. Mater. Sci.: Mater. Electron.*, 2013, **24**, 916–926.
56 M. S. Chen, Z. X. Shen, X. Y. Liu and J. Wang, *J. Mater. Res.*, 2000, **15**, 483–487.
57 P. Kubelka, *Z. Tech. Phys.*, 1931, **12**, 593–601.
58 T. Kaur, S. Kumar, B. H. Bhat, B. Want and A. K. Srivastava, *Appl. Phys. A*, 2015, **119**, 1531–1540.
59 K. Alamelu Mangai, K. Tamizh Selvi, M. Priya, M. Rathnakumari, P. Sureshkumar and S. Sagadevan, *J. Mater. Sci.: Mater. Electron.*, 2017, **28**, 1238–1246.
60 J. Mohammed, H. Y. Hafeez, T. Tchouank Tekou Carol, C. E. Ndikilar, J. Sharma, P. K. Maji, S. K. Godara and A. K. Srivastava, *Mater. Res. Express*, 2019, **6**, 056111.
61 I. A. Auwal, H. Güngüneş, A. Baykal, S. Güner, S. E. Shirsath and M. Sertkol, *Ceram. Int.*, 2016, **42**, 8627–8635.

62 G. F. Dionne, *Magnetic oxides*, Springer, New York, 2009.
63 L. Néel, *J. Phys. Radium*, 1948, **9**, 184–192.
64 W. F. Brown, *Phys. Rev.*, 1941, **60**, 139–147.
65 I. Ali, M. U. Islam, M. S. Awan, M. Ahmad, M. N. Ashiq and S. Naseem, *J. Alloys Compd.*, 2013, **550**, 564–572.
66 N. Yasmin, S. Abdulsatar, M. Hashim, M. Zahid, S. Fatima Gillani, A. Kalsoom, M. Naeem Ashiq, I. Inam, M. Safdar and M. Mirza, *J. Magn. Magn. Mater.*, 2019, **473**, 464–469.
67 G. A. Ashraf, L. Zhang, W. Abbas and G. Murtaza, *Ceram. Int.*, 2018, **44**, 18678–18685.
68 N. Yasmin, M. Mirza, S. Muhammad, M. Zahid, M. Ahmad, M. S. Awan and A. Muhammad, *J. Magn. Magn. Mater.*, 2018, **446**, 276–281.
69 N. Rezlescu, C. Doroftei, E. Rezlescu and P. D. Popa, *J. Alloys Compd.*, 2008, **451**, 492–496.
70 M. J. Iqbal and S. Farooq, *J. Alloys Compd.*, 2010, **505**, 560–567.
71 Z. Wu, R. Zhang, Z. Yu, L. Shan, L. Dong and X. Zhang, *Ferroelectrics*, 2018, **529**, 120–127.
72 M. khandani, M. Yousefi, S. S. S. Afghahi, M. M. Amini and M. B. Torbati, *Mater. Chem. Phys.*, 2019, **235**, 121722.
73 Y.-M. Kang, *Ceram. Int.*, 2015, **41**, 4354–4359.
74 Y. Yang, F. Wang, J. Shao, D. Huang, A. V. Trukhanov and S. V. Trukhanov, *Appl. Phys. A*, 2019, **125**, 37.
75 Y. Yang, F. Wang, J. Shao, D. Huang, H. He, A. V. Trukhanov and S. V. Trukhanov, *J. Alloys Compd.*, 2018, **765**, 616–623.
76 S. E. Shirsath, M. L. Mane, S. M. Patange, S. S. Jadhav and K. M. Jadhav, *J. Phys. Chem. C*, 2011, **115**, 20905–20912.
77 M. Z. Shoushtari, S. E. M. Ghahfarokhi and F. Ranjbar, *Adv. Mater. Res.*, 2012, **622–623**, 925–929.
78 B. A. Calhoun and M. J. Freiser, *J. Appl. Phys.*, 1963, **34**, 1140–1145.
79 P. W. Anderson, *Phys. Rev.*, 1950, **79**, 705–710.
80 Y. J. Yang, X. S. Liu and F. J. Feng, *Mater. Technol.*, 2014, **29**, 188–192.
81 F. M. Gu, W. W. Pan, Q. F. Liu and J. B. Wang, *J. Phys. Appl. Phys.*, 2013, **46**, 445003.
82 C. Singh, S. B. Narang, I. S. Hudiara, Y. Bai and K. Marina, *Mater. Lett.*, 2009, **63**, 1921–1924.
83 J. Singh, C. Singh, D. Kaur, H. Zaki, I. A. Abdel-Latif, S. B. Narang, R. Jotania, S. R. Mishra, R. Joshi, P. Dhruv, M. Ghimire, S. E. Shirsath' and S. S. Meena, *J. Alloys Compd.*, 2017, **695**, 1112–1121.
84 X. He, W. Zhong, S. Yan, C.-T. Au, L. Lü and Y. Du, *J. Phys. Appl. Phys.*, 2014, **47**, 235002.
85 T. L. Phan, N. Tran, H. H. Nguyen, D. S. Yang, N. T. Dang and B. W. Lee, *J. Alloys Compd.*, 2019, **816**, 152528.
86 P. M. Md Gazzali and G. Chandrasekaran, *J. Mater. Sci.: Mater. Electron.*, 2014, **25**, 702–709.
87 I. Ali, M. U. Islam, M. S. Awan and M. Ahmad, *J. Alloys Compd.*, 2013, **547**, 118–125.
88 J. Liu and X. Xue, *Mater. Lett.*, 2016, **164**, 579–582.
89 A. D. Volodchenkov, S. Ramirez, R. Samnakay, R. Salgado, Y. Kodera, A. A. Balandin and J. E. Garay, *Mater. Des.*, 2017, **125**, 62–68.
90 G. A. Al-Garalleh, I. Bsoul, Y. Maswadeh, E. Al-Hwaitat and S. H. Mahmood, *Appl. Phys. A*, 2019, **125**, 467.
91 K. Alamelu Mangai, S. K. Tamizh and M. Priya, *J. Supercond. Novel Magn.*, 2020, **33**, 713–720.
92 Z. F. Zi, Y. P. Sun, X. B. Zhu, Z. R. Yang, J. M. dai and W. H. Song, *J. Magn. Magn. Mater.*, 2008, **320**, 2746–2751.
93 V. Harikrishnan, R. E. Vizhi, D. Rajan Babu and P. Saravanan, *J. Magn. Magn. Mater.*, 2018, **448**, 243–249.
94 F. Tran, P. Blaha, K. Schwarz and P. Novák, *Phys. Rev. B: Condens. Matter Mater. Phys.*, 2006, **74**, 155108.
95 B. C. Brightlin and S. Balamurugan, *J. Supercond. Novel Magn.*, 2017, **30**, 215–225.
96 M. A. Almessiere, Y. Slimani and A. Baykal, *Ceram. Int.*, 2018, **44**, 9000–9008.
97 I. A. Auwal, A. Baykal, S. Güner, M. Sertkol and H. Sözeri, *J. Magn. Magn. Mater.*, 2016, **409**, 92–98.
98 G. A. Ashraf, L. Zhang, W. Abbas and G. Murtaza, *Curr. Appl. Phys.*, 2019, **19**, 506–515.